Chapter 3 Chaos in Planar Attitude Motion of Spacecraft

Abstract The chaos of spacecraft in planar attitude motion is discussed in this chapter. A rigid-body spacecraft in elliptic orbit considering the gravitational and damping torque is discussed, and the Melnikov's theory is applied to predict the transverse heteroclinic point. The numerical simulations and Poincaré maps are performed to confirm the existence of chaos. The same methods are used to analyze the motion of a tethered satellite in circular orbit considering the gravitational torque and the elastic deformation of the tether, as well as a magnetic rigid spacecraft in elliptic orbits under the action of gravitational and magnetic field of the Earth. The numerical results not only confirm the existence of chaotic motion, but also serve as examples of geometrical structure of chaos, routes to chaos, and numerical identification of chaos.

Keywords planar attitude motion, rigid-body spacecraft, tethered satellites, Melnikov theory, routes to chaos, Poincaré map, Lyapunov exponents, power spectra

This chapter deals with chaos in planar attitude motion of spacecraft. The models of spacecraft treated here are rigid-body spacecraft in elliptic orbits and tethered satellites in circular orbits in the gravitational field of the Earth, as well as magnetic rigid spacecraft in circular and elliptic orbits in the gravitational and magnetic field of the Earth. For each model, previous related research results are summarized to present the necessary background, the governing equations are derived from spacecraft dynamics surveyed in chapter 1, the Melnikov theory introduced in Section 2.3 is applied to predict transverse heteroclinic points, and numerical simulations are performed employing methods described in Sections 2.1 and 2.2. The computations not only confirm the existence of chaotic motion, but also demonstrate the transition from periodic motion to chaos. Actually, these numerical results can also serve as examples of geometrical structure of chaos, routes to chaos, and numerical identification of chaos.

Y. Liu et al., *Chaos in Attitude Dynamics of Spacecraft*

3.1 Rigid Spacecraft in an Elliptic Orbit

3.1.1 Introduction

Since 1989 [1-3], much work has been done on the simplest spacecraft model with chaotic behaviors, the planar libration of a rigid body spacecraft in an elliptic orbit in the gravitational field of the Earth. If no disturbances are taken into consideration, the motion is governed by Eq. (1.3.26). If the disturbances are modeled, there will be additional small terms in the governing equation. Those disturbances include atmosphere resistance [2, 4], internal damping [4], tidal moments [5-7], Earth oblateness [3], the Earth magnetic field, third body gravitation [5, 6, 8-12], the solar-radiation pressure [12], and the control inputs [13-15]. The interaction of the magnetic field will be treated in Section 3.4.

For the cases without any disturbances, Gouliaev, Zubritska and Koshkin constructed the universal sequences of the period-doubling bifurcations for the periodic attitude motion generated from the stable state [1]. They also studied the case generated from the unstable state [16]. Gouliaev and Zavrazhina further built the scaling function to describe the spacecraft phase trajectory evolution at transition to chaos [17]. Tong and Rimrott used the Melnikov method to show that chaos occurs for all values of the system parameters and then numerically studied the dynamics for a range of orbital eccentricities and inertia ratios [18]. Karasopoulos and Richardson showed bifurcation diagrams to reveal the dependence on eccentricity, especially the transition to chaos with increasing eccentricity [19]. Teofilatto and Graziani used the Melnikov method to explain the transition from regular to chaos and numerically documented the overlapping of resonances arising both for nearly circular and highly eccentric orbits [20]. Kirchgraber, Manz, Stoffer employed “shadowing”, a mathematical technique, to prove rigorously the existence of chaos in amplitude motion of a dumbbell spacecraft [21].

There are also some investigations on the planar libration of a rigid body spacecraft in an elliptic orbit under certain disturbances. Considering atmosphere resistance, Seisl and Steindl applied the Melnikov method to present the condition of appearing chaos confirmed via numerical simulations [2]. Koch and Bruhn studied a nonspherical spacecraft whose center of mass moves in an elliptic orbit around an oblate axially symmetric central body, and used the Melnikov method to reveal that the attitude motion is chaotic for all values of the orbital eccentricity and the oblateness of the central body [3]. Chen and Liu considered both atmosphere resistance and internal damping and derived the analytical condition of occurring chaos from the Melnikov method [4]. Beletsky, Pivovarov and Starostin treated tidal moments as a dissipative factor and performed numerical simulations to explain the capture of natural celestial bodies in resonance rotation modes [6]. Khan, Sharma and Saha considered the effects of tidal moments via

the Melnikov method, and established the condition of occurring chaos [7]. Beletsky, Pivoarov and Starostin also investigated numerically chaotic attitude motion of a celestial body in gravitational field of two centers, assuming that the body moves in a circular orbit [6]. Ashenberg extended the investigation to the global dynamics in the elliptic orbit [9]. Bhardwaj and Bhatnagar applied the Melnikov method to a satellite in an elliptical orbit under the influence of third body torque and used the Chrikov criterion [22] to estimate the half-width of the chaotic separatrix [10]. Bhardwaj and Tuli presented graphically Melnikov's function in the Earth-Moon-Artificial Satellite (1958 B2 Vanguard 1) System [11]. Mehra and Bhatnagar considered both solar radiation pressure and 3rd body torque via the Melnikov analysis [12]. Gray and Stabb introduced damping and other effects to Eq. (1.3.26) through the addition of proportional-integral-derivative control, and employed a generalization of the Melnikov method to systems with slowly-varying parameters [45] to obtain the surface defining the boundary between chaotic and regular motion in physical and control parameters [13, 14]. The outcomes were compared with numerical results [15].

In this section, planar libration of a rigid-body spacecraft in an elliptic orbit with air drag and internal damping will be considered. The disturbing terms are added into the governing equation. The Melnikov analysis is performed to derive the condition of transverse heteroclinic points. Some mathematical details are included to demonstrate the application of the Melnikov theory. Numerical examples with periodic motion and chaotic motions are presented.

3.1.2 Dynamical Model

As shown in Fig. 3.1, an arbitrarily shaped rigid body spacecraft, whose principal inertia moments are A, B and C, moves in an elliptic orbit with one principal axis z normal to the orbital plane XY. Without loss of generality, suppose that $B>A$. Denote that φ is the libration angle in the orbital plane as measured from the local vertical, ν is the position angle of the spacecraft in its orbit as measured from perigee, r is the distance between the spacecraft mass center and the Earth mass center, μ is the gravitational attraction constant of the Earth. Assume that the internal

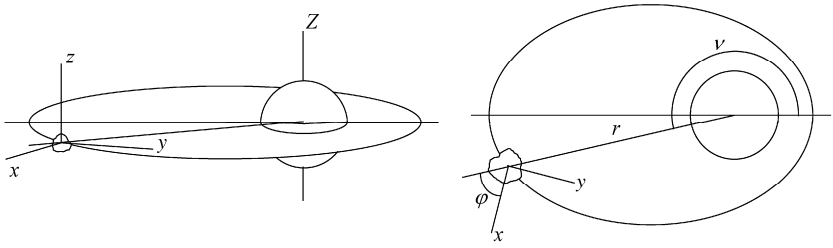

Figure 3.1 Planar motion of spacecraft in an elliptic orbit

damping and the atmosphere resistance are proportional to angular velocity and to the quadratic of angular velocity respectively, whose coefficients are γ and c.

Projection of the Euler equation in the z-direction leads to

$$\frac{\mathrm{d}}{\mathrm{d}t}\left(\frac{\mathrm{d}\nu}{\mathrm{d}t}+\frac{\mathrm{d}\varphi}{\mathrm{d}t}\right)=\frac{3\mu}{Cr^3}(B-A)\cos\varphi(-\sin\varphi)-c\frac{\mathrm{d}\varphi}{\mathrm{d}t}\left|\frac{\mathrm{d}\varphi}{\mathrm{d}t}\right|-\gamma\frac{\mathrm{d}\varphi}{\mathrm{d}t} \tag{3.1.1}$$

The orbital motion and the attitude motion are assumed to be decoupled. Thus the spacecraft moves in the Keplerian orbit defined by Eq. (1.3.24). Substitution of Eqs. (1.3.24) and (1.3.25) into Eq. (3.1.1) yields

$$\ddot{\varphi}-\frac{2e\sin\nu(1+\dot{\varphi})}{1+e\cos\nu}+\frac{\kappa\sin 2\varphi}{1+e\cos\nu}+c\dot{\varphi}|\dot{\varphi}|+\frac{\gamma\dot{\varphi}}{(1+e\cos\nu)^2}=0 \tag{3.1.2}$$

where e is the orbit eccentricity, $\kappa = 3(B-A)/(2\mathrm{C})$, and the over-dot denotes the derivative with respect to the position angle ν.

3.1.3 Melnikov Analysis

Since e, c, and γ are all small, introduce a dimensionless small parameter $\varepsilon\,(0<\varepsilon\ll 1)$ such that $e=\varepsilon e_1$, $c=\varepsilon c_1$, $\gamma=\varepsilon\gamma_1$. When the terms higher than second order of ε are omitted the Eq. (3.1.2) becomes an integrable Hamiltonian system under small perturbations

$$\ddot{\varphi}+\kappa\sin 2\varphi=\varepsilon\left[2e_1\sin\nu(1+\dot{\varphi})+e_1\kappa\cos\nu\sin 2\varphi-c_1\dot{\varphi}|\dot{\varphi}|-\gamma_1\dot{\varphi}\right] \tag{3.1.3}$$

If $\varepsilon=0$, Eq. (3.1.3) reduces to the unperturbed planar Hamiltonian system, which is essentially the same as Eq. (1.3.15),

$$\ddot{\varphi}+\kappa\sin 2\varphi=0 \tag{3.1.4}$$

with first integral of motion given by Eq. (1.3.16)

$$\frac{1}{2}\dot{\varphi}^2+\kappa\sin^2\varphi=C_0 \tag{3.1.5}$$

where C_0 is a constant. When $C_0=\kappa$, Eq. (3.1.5) has two hyperbolic saddle points $(\pm\pi/2,\ 0)$, whose unstable manifolds and stable manifolds constitute a heteroclinic cycle defined by

$$\frac{1}{2}\left(\frac{\mathrm{d}\varphi}{\mathrm{d}\nu}\right)^2+\kappa\sin^2\varphi=\kappa \tag{3.1.6}$$

Suppose that $\varphi(0)=0$. Then $\dot{\varphi}(0)=\pm\sqrt{2\kappa}$. Integration of Eq. (3.1.6) leads to

$$\int_0^{\varphi} \frac{\mathrm{d}\varphi}{\pm\sqrt{\kappa - \kappa\sin^2\varphi}} = \nu \tag{3.1.7}$$

Evaluation of the finite integral in Eq. (3.1.7) and rearrangement of terms in the resulting equation yields

$$\varphi_{\pm}(\nu) = \pm\arcsin(\mathrm{th}(\sqrt{2\kappa}\nu)) \tag{3.1.8}$$

Therefore the heteroclinic orbits $\Gamma^{\pm}$ started at $(0, \pm\sqrt{2\kappa})$ are

$$(\varphi_{\pm}(\nu), \dot{\varphi}_{\pm}(\nu)) = (\pm\arcsin(\mathrm{th}(\sqrt{2\kappa}\nu)), \pm\sqrt{2\kappa}\,\mathrm{sech}(\sqrt{2\kappa}\nu)) \tag{3.1.9}$$

For $\varepsilon \neq 0$, Eq. (3.1.3) can be cast into the form of Eq. (2.3.4) with

$$\begin{gathered} \boldsymbol{x} = \begin{pmatrix} \varphi \\ \dot{\varphi} \end{pmatrix}, \quad \boldsymbol{f}(\boldsymbol{x}) = \begin{pmatrix} \dot{\varphi} \\ \kappa\sin 2\varphi \end{pmatrix} \\ \boldsymbol{g}(\boldsymbol{x}, \nu) = \begin{pmatrix} 0 \\ 2e_1\sin\nu(1+\dot{\varphi}) + e_1\kappa\cos\nu\sin 2\varphi - c_1\dot{\varphi}\left|\dot{\varphi}\right| - \gamma_1\dot{\varphi} \end{pmatrix} \end{gathered} \tag{3.1.10}$$

The unperturbed system (3.1.4) is Hamiltonian, and thus $\mathrm{tr}(\mathbf{D}\boldsymbol{f}) = 0$. Application of Eq. (2.3.26) yields

$$\begin{aligned} \mathcal{M}_{\pm}(\nu_0) = \int_{-\infty}^{+\infty} \big[& 2e_1\sin(\nu+\nu_0)(1+\dot{\varphi}_{\pm}(\nu)) + e_1\kappa\cos(\nu+\nu_0)\sin 2\varphi_{\pm}(\nu) \\ & - c_1\dot{\varphi}_{\pm}(\nu)\left|\dot{\varphi}_{\pm}(\nu)\right| - \gamma_1\dot{\varphi}_{\pm}(\nu)\big]\dot{\varphi}_{\pm}(\nu)\,\mathrm{d}\nu \end{aligned} \tag{3.1.11}$$

Notice that the integral of an odd function over a symmetrical interval is zero. Equation (3.1.11) can be simplified to

$$\mathcal{M}_{\pm}(\nu_0) = 2e_1 I_1\sin\nu_0 + 2e_1 I_2\sin\nu_0 + e_1\kappa I_3\sin\nu_0 - c_1 I_4 - \gamma_1 I_5 \tag{3.1.12}$$

where

$$I_1 = \int_{-\infty}^{+\infty} \cos\nu\,\dot{\varphi}_{\pm}(\nu)\,\mathrm{d}\nu \tag{3.1.13}$$

$$I_2 = \int_{-\infty}^{+\infty} \cos\nu\,\dot{\varphi}_{\pm}^{\,2}(\nu)\,\mathrm{d}\nu \tag{3.1.14}$$

$$I_3 = \int_{-\infty}^{+\infty} \sin\nu\sin 2\varphi_{\pm}(\nu)\dot{\varphi}_{\pm}(\nu)\,\mathrm{d}\nu \tag{3.1.15}$$

$$I_4 = \int_{-\infty}^{+\infty} \dot{\varphi}_{\pm}^{\,2}(\nu)\left|\dot{\varphi}_{\pm}(\nu)\right|\mathrm{d}\nu \tag{3.1.16}$$

$$I_5 = \int_{-\infty}^{+\infty} \dot{\varphi}_{\pm}^{\,2}(\nu)\,\mathrm{d}\nu \tag{3.1.17}$$

Substitution of Eq. (3.1.9) into Eqs. (3.1.13)-(3.1.15) and application of the theorem of residues to suitably constructed contours for I_1, I_2, and I_3 yield

$$I_1 = \pm\pi \operatorname{sech}\frac{\pi}{2\sqrt{2K}} \tag{3.1.18}$$

$$I_2 = \pi \operatorname{csch}\frac{\pi}{2\sqrt{2K}} \tag{3.1.19}$$

$$I_3 = -\frac{1}{4}\pi \operatorname{csch}\frac{\pi}{2\sqrt{2K}} \tag{3.1.20}$$

Application of Eq. (3.1.6) and the change of variable in I_4 and I_5 give

$$\begin{aligned} I_4 &= \int_{-\frac{\pi}{2}}^{\frac{\pi}{2}} \dot{\varphi}_\pm \left|\dot{\varphi}_\pm\right| \mathrm{d}\varphi_\pm = \pm\int_{\mp\frac{\pi}{2}}^{\pm\frac{\pi}{2}} \sqrt{2\kappa(1-\sin^2\varphi_\pm)}\left|\sqrt{2\kappa(1-\sin^2\varphi_\pm)}\right| \mathrm{d}\varphi_\pm \\ &= 2\kappa\int_{-\frac{\pi}{2}}^{\frac{\pi}{2}} \cos^2\varphi_\pm \,\mathrm{d}\varphi_\pm = \kappa\pi \end{aligned} \tag{3.1.21}$$

$$I_5 = \int_{\mp\frac{\pi}{2}}^{\pm\frac{\pi}{2}} \dot{\varphi}_\pm \,\mathrm{d}\varphi_\pm = \pm\int_{\mp\frac{\pi}{2}}^{\pm\frac{\pi}{2}} \sqrt{2\kappa(1-\sin^2\varphi_\pm)}\,\mathrm{d}\varphi_\pm = \sqrt{2\kappa}\int_{-\frac{\pi}{2}}^{\frac{\pi}{2}} \cos\varphi_\pm \,\mathrm{d}\varphi_\pm = 2\sqrt{2\kappa}\,\pi \tag{3.1.22}$$

Therefore, Eq. (3.1.11) becomes

$$\mathcal{M}_\pm(\nu_0) = \frac{\pi}{2}e_1\left(\mp 4\operatorname{sech}\frac{\pi}{2\sqrt{2\kappa}} + 3\operatorname{csch}\frac{\pi}{2\sqrt{2\kappa}}\right)\sin\nu_0 - \pi c_1\kappa - 2\sqrt{2\kappa}\pi\gamma_1 \tag{3.1.23}$$

If both $\mathcal{M}_+(\nu_0)$ and $\mathcal{M}_-(\nu_0)$ have simple zeros, then there exists a transverse heteroclinic point in the Poincaré map of Eq. (3.1.2). Notice $|\sin\nu_0| \leqslant 1$, if and only if

$$e > \frac{2c\kappa + 4\sqrt{2\kappa}\gamma}{\left|3\operatorname{csch}\dfrac{\pi}{2\sqrt{2\kappa}} - 4\operatorname{sech}\dfrac{\pi}{2\sqrt{2\kappa}}\right|} \tag{3.1.24}$$

Thus the transverse heteroclinic point exists.

3.1.4 Numerical Simulations

Fix $\kappa = 0.75$, $\gamma = 0.05$, and $c = 0.04$ in Eq. (3.1.2). Varying e may result in

periodic or chaotic motion. For example, If e is very small, the attitude motion is periodic The case with $e = 0.080$ is shown in Fig. 3.2. The attitude motion chaotic motion appears if $e = 0.085$, and the time history and the phase trajectory are separately shown in Fig. 3.3.

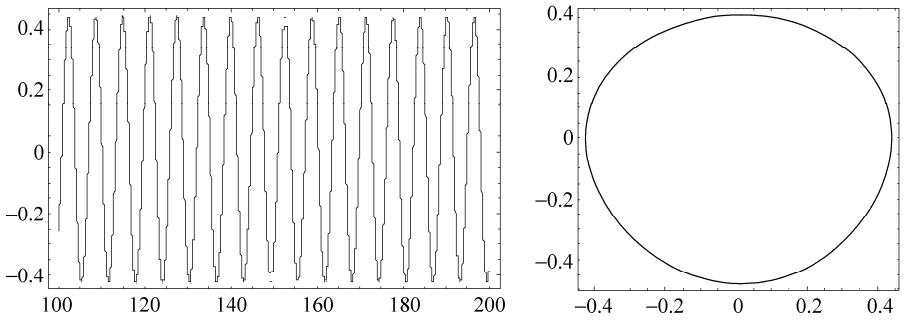

Figure 3.2 Periodic attitude motion of a rigid spacecraft in an elliptic orbit

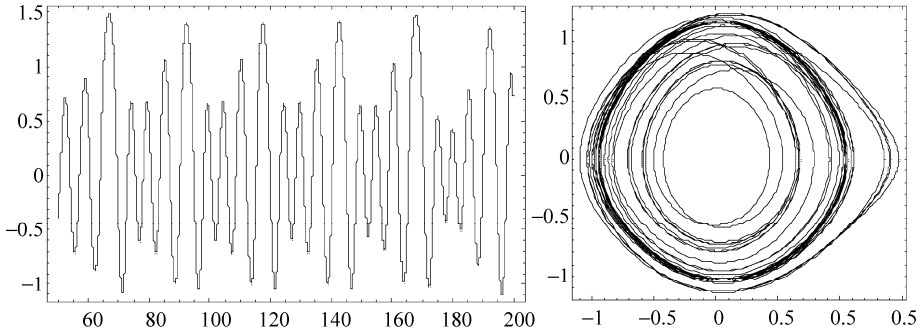

Figure 3.3 Chaotic attitude motion of a rigid spacecraft in an elliptic orbit

3.2 Tethered Satellite Systems

3.2.1 Introduction

A system of two or more subsatellites connected by a long cable is called a tethered satellite system. Tethered satellite systems have many applications in space exploration and development because tethers can be used to construct large-scale space structures. The study of the motion of tethered satellite systems is a challenging new field in spacecraft dynamics [23].

In 1993, Nixon and Misra first considered the possibility of chaotic motion in a two-body tethered satellite system with a rigid tether [24]. For a two-body tethered satellite system moving in a circular orbit, Peng and Liu applied the Melnikov method to predict chaos and performed numerical simulations to demonstrate periodic and chaotic motions in the case of decoupled longitudinal tether vibration, and also studied numerically the coupled case [25]. On the assumption that the center moves in an elliptic orbit and the tether is an ideally flexible mass-less inextensible thread, Béda numerically studied a two-body tethered satellite system subjected to the aerodynamical forces, and found chaotic regions in the parameter space [26]. For a linear spring connected two-body satellite system moving in an elliptical orbit, Fujji and Ichiki used Poincaré maps, bifurcation diagrams, and maximum Lyapunov exponents to demonstrate that chaos occurs for low tether elasticity and large orbit eccentricity [27]. For viscoelastically tethered satellite systems with two stable radial and two unstable tangent-to-orbit equilibria, Steiner employed the finite-element method to show numerically that asymptotic behavior of the transient chaotic motion strongly depended on the choice of initial conditions and that final equilibria on which it settled down are unpredictable for initial conditions near an unstable equilibrium [28, 29]. Beletsky and Pivovarov investigated numerically a tethered satellite system acted upon by gravitational and aerodynamic forces, and found that the aero-gradient effect may result in strong spinup of the system and the orbit eccentricity may lead to chaotic motion [30]. Based on the equations governing the three-dimensional motion of a two-body satellite system, Misra, Nixon and Modi observed numerically the existence of both regular and chaotic regions in the planar system for only elliptic orbits, but in the case of 3-dimensional motion for both circular and elliptic orbits they found that the size of the chaotic region grows with eccentricity, and in the 3-dimensional motion circular orbit case, it grows with increasing values of the Hamiltonian [31]. Takeichi, Natori and Okuizumi numerically simulated dynamic behavior of a tethered system with multiple subsatellites subjected to both atmospheric drag and changes of gravity gradient in elliptic orbits [32].

This section is devoted to chaotic attitude motion of a tethered satellite system. A dynamical model is developed on the assumption that the longitudinal vibration of tether is small and uncoupled from the attitude motion. The coupled model is also derived from the Hamiltonian equation. The Melnikov theory is applied to the uncoupled case. Numerical simulations are performed for both models.

3.2.2 Dynamical Models

Assume that each segment of a tethered satellite system is simplified as a mass point moving synchronously in a circular orbit, and the tether is stretched as a straight line as shown in Fig. 3.4.

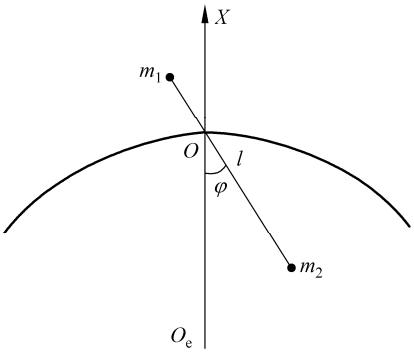

Figure 3.4 Tethered satellite

Let $m_i (i = 1,2)$ be the masses of segments and l be the length of the tether. Then the distance l_i of each segment $m_i (i = 1,2)$ to mass center O can be derived as

$$l_1 = \left(\frac{m_2}{m_1 + m_2} \right) l, \quad l_2 = \left(\frac{m_1}{m_1 + m_2} \right) l \tag{3.2.1}$$

Define the body-fixed frame O-xyz with Ox along the tether from m_2 to m_1, and Oz coincident with the normal axis of the orbital plane. Then the principal moments of inertia of the satellite with the mass-less tether about point O are

$$A = 0, \ B = C = m^* l^2 \tag{3.2.2}$$

where $m^* = m_2 m_1/(m_2 + m_1)$. The dynamical equation of planar libration with swing angle φ can be derived from the theorem of angular momentum (1.3.2).

The elastic deformation of the tether is specified by its length $l(t)$, which is a function of time. The gravitational torque on the tethered satellite is given by Eq. (1.3.13). Then one obtains

$$\ddot{\varphi} + \left(\frac{2\dot{l}}{l} \right) (\dot{\varphi} + \omega_c) + \left(\frac{3\omega_c^2}{2} \right) \sin 2\varphi = 0 \tag{3.2.3}$$

If the variation of the tether length is small, the coupling between the attitude motion and the longitudinal vibration of tether can be neglected. Thus it can be assumed that the longitudinal vibration of tether is described by

$$l = l_0 + \Delta l \cos \omega_0 t \tag{3.2.4}$$

where l_0 is the original length of the tether, Δl and ω_0 are the amplitude and the frequency of its vibration, respectively. Introduce the dimensionless time τ, and dimensionless parameters δ and ε as

$$\tau = \omega_0 t,\ \delta = \frac{\omega_c}{\omega_0},\ \varepsilon = \frac{\Delta l}{l_0} \tag{3.2.5}$$

Equation (3.2.3) can be cast into the dimensionless form as

$$\ddot{\varphi} - 2\varepsilon(\dot{\varphi} + \delta)\sin\tau + \frac{3}{2}\delta^2 \sin 2\varphi = 0 \tag{3.2.6}$$

where the derivative is with respect to the dimensionless time.

When the longitudinal displacement of the tether is quite large, the swing and the longitudinal vibration are strongly coupled, and the system should be regarded as possessing two degrees of freedom. The kinetic energy of the system is

$$T = \frac{1}{2}\left[m^* \left(\dot{l}^2 + l^2\dot{\varphi}^2 \right) + \left(m_1 + m_2 \right) v_c^2 \right] \tag{3.2.7}$$

The potential energy of gravitational field is derived from Eq. (1.3.40) in which

$$\alpha_1 = \cos\varphi,\ \alpha_2 = \sin\varphi,\ \alpha_3 = 0 \tag{3.2.8}$$

as

$$V_1 = \frac{3}{2}\omega_c^2 m^* l^2 \sin^2\varphi \tag{3.2.9}$$

Denote the coefficient of tether stiffness by K, then the potential energy of the elastic tether deformation is

$$V_2 = \frac{1}{2}K(l - l_0)^2 \tag{3.2.10}$$

According to Eq. (1.3.41), omitting the constant terms and dividing it by $m^*\omega_0^2 l_0$, one obtains the normalized Hamiltonian of the system as

$$H = \frac{1}{2}\left[\left(\frac{\mathrm{d}\xi}{\mathrm{d}\tau} \right)^2 + (1+\xi)\left(\frac{\mathrm{d}\varphi}{\mathrm{d}\tau} \right)^2 + 3\delta\xi^2 \sin^2\varphi \right] + \frac{1}{2}k\xi^2 \tag{3.2.11}$$

where k is the dimensionless stiffness coefficient and ξ is a new variable defined as

$$k = \frac{K}{m^*\omega_0^2 l_0},\quad \xi = \frac{l - l_0}{l_0} \tag{3.2.12}$$

The dynamical equations of the system can be written in canonical form, where the generalized momenta are defined as

$$p_\varphi = (1+\xi)\frac{\mathrm{d}\varphi}{\mathrm{d}\tau},\quad p_\xi = \frac{\mathrm{d}\xi}{\mathrm{d}\tau} \tag{3.2.13}$$

Thus the Hamiltonian equations yield

$$\begin{aligned}
\frac{\mathrm{d}\varphi}{\mathrm{d}\tau} &= \frac{\partial \mathcal{H}}{\partial p_\varphi} = p_\varphi \\
\frac{\mathrm{d}p_\varphi}{\mathrm{d}\tau} &= -\frac{\partial \mathcal{H}}{\partial \varphi} = -\frac{3}{2}\delta\xi^2 \sin 2\varphi \\
\frac{\mathrm{d}\xi}{\mathrm{d}\tau} &= \frac{\partial \mathcal{H}}{\partial p_\xi} = p_\xi \\
\frac{\mathrm{d}p_\xi}{\mathrm{d}\tau} &= -\frac{\partial \mathcal{H}}{\partial \xi} = -\frac{1}{2}\left(\frac{p_\varphi}{1+\xi}\right)^2 - 3\delta\xi\sin^2\varphi - k\xi
\end{aligned} \tag{3.2.14}$$

3.2.3 Melnikov Analysis of the Uncoupled Case

Equation (3.2.6) is established on the supposition that Δl is small. Thus ε, defined by Eq. (3.2.5), can be regarded as a small parameter. Consequently, Eq. (3.2.6) is an integrable Hamiltonian system experiencing small perturbations

$$\ddot{\varphi} + \frac{3}{2}\delta^2 \sin 2\varphi = 2\varepsilon(\dot{\varphi} + \delta)\sin\tau \tag{3.2.15}$$

If $\varepsilon = 0$, Eq. (3.2.15) becomes Eq. (3.1.4), in which $\kappa = 3\delta^2/2$. The unperturbed system has two hyperbolic saddle points $(\pm\pi/2, 0)$ connected by the heteroclinic orbits $\Gamma^{\pm}$ obtained from Eq. (3.1.9).

$$(\varphi_\pm(\tau), \dot{\varphi}_\pm(\tau)) = (\pm\arcsin(\mathrm{th}(\sqrt{3}\delta\tau)), \pm\sqrt{3}\delta\,\mathrm{sech}(\sqrt{3}\delta\tau)) \tag{3.2.16}$$

For $\varepsilon \neq 0$, Eq. (3.2.15) can be written in the form of Eq. (2.3.4) with

$$\boldsymbol{x} = \begin{pmatrix} \varphi \\ \dot{\varphi} \end{pmatrix}, \quad \boldsymbol{f}(\boldsymbol{x}) = \begin{pmatrix} \dot{\varphi} \\ \kappa \sin 2\varphi \end{pmatrix}, \quad \boldsymbol{g}(\boldsymbol{x}, \tau) = \begin{pmatrix} 0 \\ 2(\dot{\varphi} + \delta)\sin\tau \end{pmatrix} \tag{3.2.17}$$

Equation (2.3.26) yields

$$\mathcal{M}_\pm(\tau_0) = \int_{-\infty}^{+\infty} \left[2(\dot{\varphi}_\pm(\tau) + \delta)\sin(\tau + \tau_0)\right]\dot{\varphi}_\pm(\tau)\,\mathrm{d}\tau \tag{3.2.18}$$

Substitution of Eq. (3.2.16) into Eq. (3.2.18) and evaluation of the resulting integrals in a similar way in 3.1.3 leads to the Melnikov function

$$\mathcal{M}(\tau_0) = \mathcal{M}_0 \sin\tau_0 \tag{3.2.19}$$

where $\mathcal{M}_0$ is a constant

$$\mathcal{M}_0 = -2\pi\left(\operatorname{csch}\frac{\pi}{2\sqrt{3}\delta} + \delta\operatorname{sech}\frac{\pi}{2\sqrt{3}\delta}\right) \tag{3.2.20}$$

Hence the function $\mathcal{M}(\tau_0)$ always possesses simple zeros.

3.2.4 Numerical Simulations

Equation (3.2.6) is integrated by use of the numerically integration algorithm so that the Poincaré map defined as $(\varphi(2k\pi), \dot{\varphi}(2k\pi))\ (k = 1, 2, \cdots)$ can be computed. To obtain a global view of the system dynamics, the Poincaré maps from different initial conditions are put together to form a global Poincaré map. Figure 3.5 shows a global Poincaré map for Eq. (3.2.6) starting at 30 different initial conditions for different parameters. The two different types of motion, regular and chaotic,

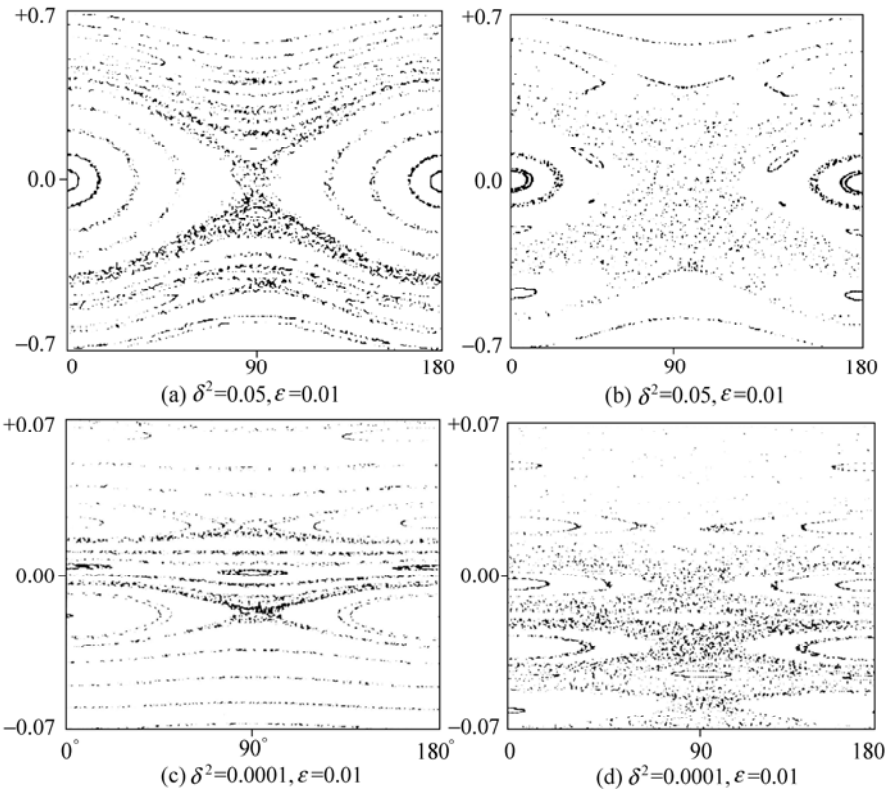

Figure 3.5 The global Poincaré map of a tethered satellite: uncoupled case

are readily distinguished on the Poincaré maps. For the regular motion, successive points describe smooth curves or separate points, and for the chaotic motion, the points fill an area in apparently random manner. In Fig. 3.5(a) for a rather small ε, the Poincaré map is fairly well covered by invariant tori. It indicates that most of the motions are periodic or quasi-periodic. With increasing ε some tori break into chaotic trajectories in the sense that successive points on Poincaré map do not lie on a curve anymore, but densely fill an area. One can also see a hyperbolic point and homoclinic orbits connected to it, and the small region close to the separatrix is covered by chaotic trajectories as shown in Fig. 3.5 (b), (c), and (d).

For the case of coupled motion, Eq. (3.2.14) is numerically integrated for 4 different initial conditions. The resulting Poincaré maps in the (φ, p_φ) plane are shown in Fig. 3.3. In Fig. 3.3(a), for a low energy level, most of the Poincaré maps are fairly well covered by invariant tori indicating that most of the periodic and quasi-periodic motions are preserved. With increasing $\mathcal{H}$ some tori break into chaotic trajectories (see Fig. 3.3(b)~(d)), and for further increasing $\mathcal{H}$, regular motion gradually disappears finally ending in a chaotic ocean as shown in Fig. 3.3(e) and 3.3(f).

3.3 Magnetic Rigid Spacecraft in a Circular Orbit

3.3.1 Introduction

In addition to the gravitational torque, the magnetic torque plays a significant role in attitude motion of a magnetized spacecraft. In fact, gravitational and magnetic forces are dominant environmental effects for spacecraft moving at an altitude higher than 500 km [33]. This section begins to discuss chaotic attitude motion in the gravitational and magnetic fields, while the discussions here are limited to the case of spacecraft moving in a circular orbit.

Beletsky *et al.* investigated numerically chaotic attitude motion of a magnetic satellite in a circular orbit in the absence of a gravitational moment, and found that chaotization increases with the growth of the magnetic parameter [5, 6]. Bhardwaj and Bhatnagar applied the Melnikov method to rotational motion of a satellite in a circular orbit under the influence of magnetic torque [34]. They also used the Chrikov criterion [22] to estimate the chaotic separatrix and employed Poincaré map to highlight the important role of the magnetic torque and the mass distribution in changing the regular motion into chaos [35]. Beletsky, Lopes and Pivovarov studied the global phase portrait of a permanent magnetic satellite moving in a circular orbit without the gravitational moment and compared the chaotic region with its theoretical boundary obtained by the adiabatic approximation [36]. For the planar motion of a magnetic rigid spacecraft moving in a circular

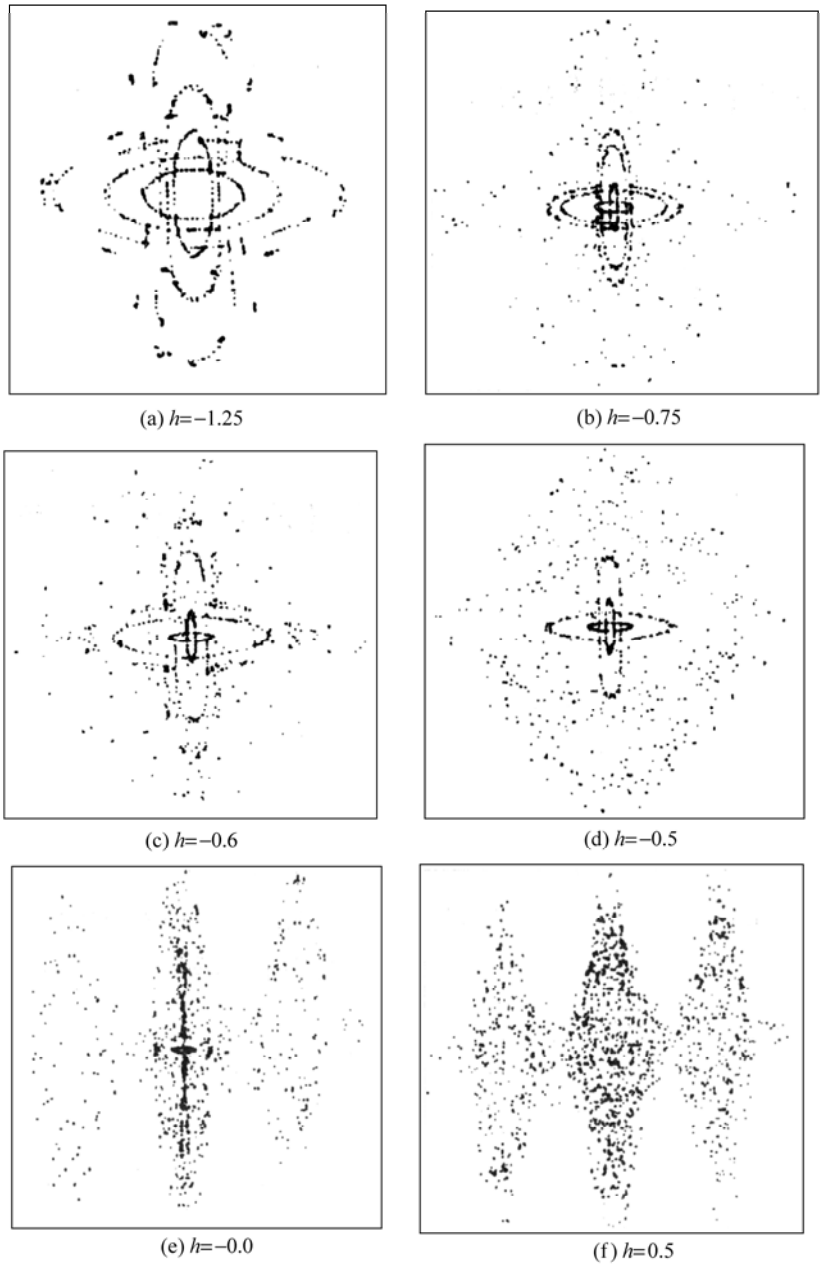

Figure 3.6 The global Poincaré map in plane (φ, p_φ) of a tethered satellite: coupled case

orbit near the equatorial plane of the Earth under the action of the gravitational and magnetic torques, Cheng and Liu found the existence of Smale's horseshoe via the Melnikov method and numerically demonstrated the intensification of chaos due to periodic disturbance of the magnetic field [37]. These investigations [5, 6, 34-37] used the Poincaré maps based on the numerical solutions to identify chaos. Chen and Liu employed the Poincaré map, the power spectrum and the Lyapunov exponents to demonstrate that the onset of chaos in a model developed in [37] is characterized by a breakup of torus as the torque of the magnetic forces is increased [38]. Considering the internal damping, which is an addition to the Melnikov analysis, Chen and Liu numerically investigated a magnetic rigid spacecraft in a circular orbit via the Poincaré map, the power spectrum and the Lyapunov exponents, and demonstrated the transition from periodic motion to chaos via intermittency as the increase of the torque of the magnetic field and the decrease of the damping [39]. Based on the Differential Galois Theory [40], Maciejewski and Przybylska proved the non-integrability of the dynamical system governing the attitude motion of a symmetric rigid satellite under the influence of gravitational and magnetic fields, with the only exception that the value of the induced magnetic moment along the symmetry axis is related to the principal moments of inertia in a special way [41].

This section treats a rigid-body spacecraft moving in a circular orbit. The dynamical model is derived from the theorem of angular momentum. The Melnikov theory is applied to predict the appearance of transverse heteroclinic points. In both undamped and damped cases, the routes to chaos are numerically examined via the Poincaré map, the power spectrum and the Lyapunov exponents. Numerical results demonstrate that the onset of chaos is characterized by the breakup of torus as the magnetic torque is increased in the undamped case and by the intermittency in the damped case as the magnetic torque is increased and the damping is decreased.

3.3.2 Dynamical Model

Consider a magnetic rigid spacecraft moving in a circular orbit with the orbital angular velocity ω_c in the gravitational and magnetic field of the Earth. Consider a magnetic rigid spacecraft moving in an elliptic orbit in the gravitational and magnetic field of the Earth. Assume that the inertial reference frame (O_e-$X_0Y_0Z_0$) has the origin O_e at the mass center of the Earth, with the polar axis of the Earth as Z_0-axis and the line from O_e to the ascending node as X_0-axis. The principal coordinate frame (O-xyz) has the mass center O as the origin. Principal moments of inertia of the arbitrarily shaped spacecraft are A, B and C. Suppose that $B>A$. The orbital coordinate frame (O-XYZ) is established with the radial vector from O_e to O as X-axis, the normal vector to orbital plane XY as Z-axis. The base vectors of (O-XYZ) are $\boldsymbol{i}$, $\boldsymbol{j}$, $\boldsymbol{k}$. Denote φ as the libration angle in the orbital plane with

respect to *X*- or *Y*-axis, and *i* as the angle of inclination of the orbital plane, all shown in Fig. 3.7. Assume that the internal damping torque $\boldsymbol{M}_{\mathrm{d}}$ is proportional to angular velocity whose coefficients is *c*. Then

$$\boldsymbol{M}_{\mathrm{d}} = -c\dot{\varphi}\boldsymbol{k} \tag{3.3.1}$$

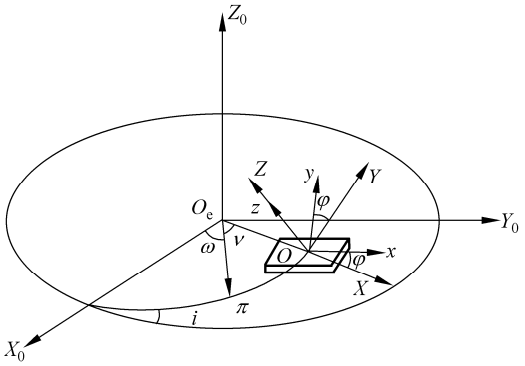

Figure 3.7 The reference frames

Application of the theorem of angular momentum to the spacecraft leads to

$$\dot{\boldsymbol{G}} = \boldsymbol{M}_{\mathrm{g}} + \boldsymbol{M}_{\mathrm{m}} + \boldsymbol{M}_{\mathrm{d}} \tag{3.3.2}$$

where $\boldsymbol{G}$ is the angular momentum, and $\boldsymbol{M}_{\mathrm{g}}$ and $\boldsymbol{M}_{\mathrm{m}}$ are the torques resulted form the gravitational and magnetic field respectively. When the orbit is circular, the gravitational torque $\boldsymbol{M}_{\mathrm{g}}$ is along the normal axis, and its magnitude is given by Eq. (1.3.12). Substitution of Eq. (1.3.14) into Eq. (1.3.12) yields

$$M_{\mathrm{g}z} = \frac{3}{2}\omega_{\mathrm{c}}^2 (B - A)\sin 2\varphi \tag{3.3.3}$$

The magnetic field is assumed to be that of a dipole with the magnetic moment whose axis coincides the Earth's axis. For the orbital plane with the inclination angle *i*, the components of the magnetic flux density $\boldsymbol{H}_{\mathrm{m}}$ of the Earth in (*O*-*XYZ*) are given by Eq. (1.2.11). Assume that the magnetic moment $\boldsymbol{I}_{\mathrm{m}}$ of the spacecraft is along *Ox* -axis and the direction of the vector $\boldsymbol{I}_{\mathrm{m}}$ in the orbital plane is specified by the angle φ as shown in Fig. 1.11. Thus the direct cosines of $\boldsymbol{I}_{\mathrm{m}}$ with respect to (*O*-*XYZ*) are ($\cos\varphi$, $\sin\varphi$, 0). When the orbit is circular, the orbital angle *u* in Eq. (1.2.11) can be written as

$$u = \omega_{\mathrm{c}} t \tag{3.3.4}$$

Substitution of Eqs. (3.3.4), (1.2.11) and the direct cosines into Eq. (1.2.14) yields the projection of the magnetic torque $\boldsymbol{H}_{\mathrm{m}}$ on *Oz*-axis as

$$M_{mz} = I_m H_{m0} \sin i(2\sin\varphi\sin\omega_c t + \cos\varphi\cos\omega_c t) \tag{3.3.5}$$

Projecting Eq. (3.3.2) on the *Oz*-axis and substituting Eqs. (3.3.1), (3.3.3) and (3.3.5) into the resulting equation, one obtains the dynamical equation in the dimensionless form

$$\ddot{\varphi} + \gamma\dot{\varphi} + \kappa\sin 2\varphi - \alpha(2\sin\varphi\sin\tau + \cos\varphi\cos\tau) = 0 \tag{3.3.6}$$

where $\tau = \omega_c t$ is defined as the dimensionless time and

$$\gamma = \frac{c}{C\omega_c}, \kappa = \frac{3(B-A)}{2C}, \alpha = \frac{IH_{m0}\sin i}{C\omega_c^2} \tag{3.3.7}$$

The derivatives in Eq. (3.3.6) are with respect to the dimensionless time τ.

3.3.3 Melnikov Analysis

Assume that both the damping coefficient γ and the magnetic parameter α are small and let $\gamma = \varepsilon\gamma_1$ and $\alpha = \varepsilon\alpha_1$ ($0<\varepsilon \ll 1$). Then Eq. (3.3.6) is an integrable Hamiltonian system under small perturbations

$$\ddot{\varphi} + \sigma\sin 2\varphi = \varepsilon\alpha_1(2\sin\varphi\sin\tau + \cos\varphi\cos\tau) - \varepsilon\gamma_1\dot{\varphi} \tag{3.3.8}$$

If $\varepsilon = 0$, Eq. (3.3.8) becomes Eq. (3.1.4) with two hyperbolic saddle points ($\pm\pi/2$, 0) connected by the heteroclinic orbits $\Gamma^{\pm}$ defined by Eq. (3.1.9). For $\varepsilon \neq 0$, Eq. (3.3.8) can be cast into the form of Eq. (2.3.4) with

$$\begin{aligned} \boldsymbol{x} &= \begin{pmatrix} \varphi \\ \dot{\varphi} \end{pmatrix}, \quad \boldsymbol{f}(\boldsymbol{x}) = \begin{pmatrix} \dot{\varphi} \\ \kappa\sin 2\varphi \end{pmatrix} \\ \boldsymbol{g}(\boldsymbol{x},\tau) &= \begin{pmatrix} 0 \\ \alpha_1\left(2\sin\varphi\sin\tau + \cos\varphi\cos\tau\right) - \gamma_1\dot{\varphi} \end{pmatrix} \end{aligned} \tag{3.3.9}$$

Equation (2.3.26) yields

$$\begin{aligned} \mathcal{M}_{\pm}(\tau_0) = \int_{-\infty}^{+\infty} \big[&-\alpha_1\left(2\sin\varphi_{\pm}(\tau)\sin(\tau+\tau_0)\right. \\ &\left. + \cos\varphi_{\pm}(\tau)\cos(\tau+\tau_0)\right) - \gamma_1\dot{\varphi}_{\pm}(\tau)\big]\dot{\varphi}_{\pm}(\tau)\,\mathrm{d}\tau \end{aligned} \tag{3.3.10}$$

Substitution of Eq. (3.1.9) into Eq. (3.3.10) and calculation of the resulting integrals in a similar fashion in 3.1.1 leads to the explicit expression of the Melnikov function

$$\mathcal{M}_{\pm}(\tau_0) = \frac{\alpha_1\pi}{2\kappa}(1+\sqrt{2\kappa})\,\mathrm{csch}\left(\frac{\pi}{2\sqrt{2\kappa}}\right)\sin\tau_0 - 2\sqrt{2}\gamma_1\kappa \tag{3.3.11}$$

For the undamped case, let $\gamma_1 = 0$, thus function $\mathcal{M}_{\pm}(\tau_0)$ always has simple zeros. For the damped case, both $\mathcal{M}_{+}(\tau_0)$ and $\mathcal{M}_{-}(\tau_0)$ have simple zeros on the condition that

$$\frac{\alpha}{\gamma} = \frac{\alpha_1}{\gamma_1} > \frac{4\sqrt{2}\kappa^2}{\pi(1+\sqrt{2}\kappa)} \operatorname{sh}\left(\frac{\pi}{2\sqrt{2K}}\right) \tag{3.3.12}$$

3.3.4 Numerical Investigations: Undamped Case

The effect of the magnetic parameter α upon the spacecraft attitude motion is now investigated numerically by integrating Eq. (3.3.6) in which $\gamma = 0$. The global view of the Poincaré map is presented by the calculation based on a set of initial conditions. Then the routes to chaos are numerically investigated for a given initial condition.

Equation (3.3.6) is numerically integrated for 7 different initial conditions. The Poincaré maps defined as $(\varphi(2k\pi), \dot{\varphi}(2k\pi))$ $(k = 1, 2, \cdots)$ are shown in Fig. 3.8 for

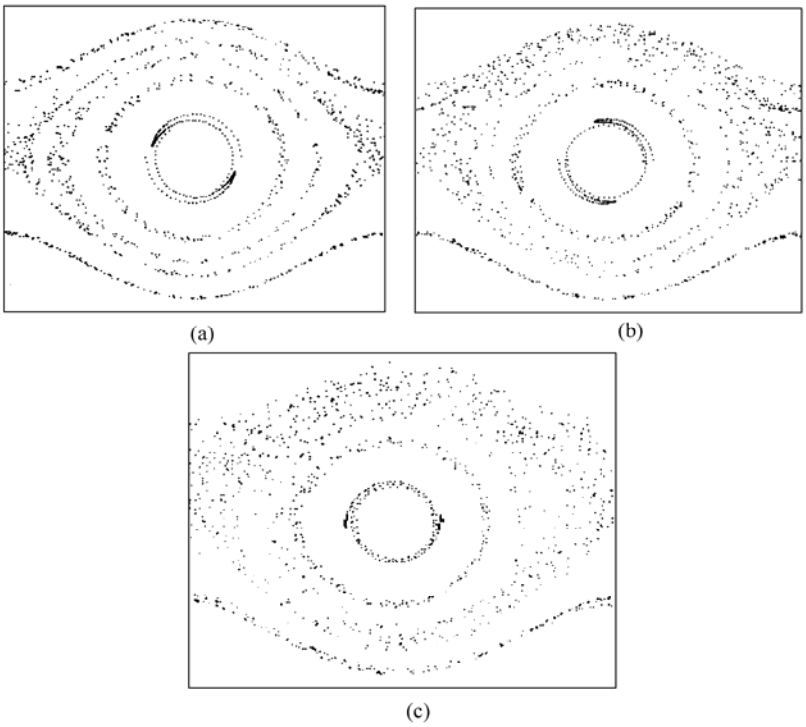

Figure 3.8 The global Poincaré maps of a magnetic spacecraft (a) $\alpha = 0.01$; (b) $\alpha = 0.02$; (c) $\alpha = 0.05$

α= 0.01, 0.02 and 0.05. It can be seen that under the action of the periodic disturbance of magnetic torque, the motion of spacecraft rapidly becomes irregular and turns into chaotic motion. As the disturbance increases, the chaotic region is enlarged.

The characteristic dynamical behavior is investigated by varying the magnetic parameter α, while the gravitational parameter κ is kept constant at $\kappa = 0.75$. The numerical integration begins from the initial condition (0,0).

When α is small enough, the system experiences quasi-periodic motion. For $\alpha = 0.01$, the time history, the Poincaré map, power spectrum and the largest Lyapunov exponent are depicted in Fig. 3.9. The Lyapunov exponents are all very close to zero.

For relatively large α, the quasi-periodic torus begin to break up. For $\alpha = 0.12$ and $\alpha = 0.1275$, the time history, the Poincaré map, power spectrum and the largest Lyapunov exponent are shown in Fig. 3.10 and Fig. 3.11, respectively. Even if those Poincaré maps were almost the same as those in Fig. 3.9, the power spectra show differences. The Lyapunov exponents are 0.00, 0.00 and 0.01, –0.01.

For sufficiently large α, the quasi-periodic torus breaks up completely and chaotic motion occurs in the system. For $\alpha = 0.1276$, the time history, the Poincare map, power spectrum and the largest Lyapunov exponent are shown in Fig. 3.12. The Lypunov exponents are 0.12, –0.12.

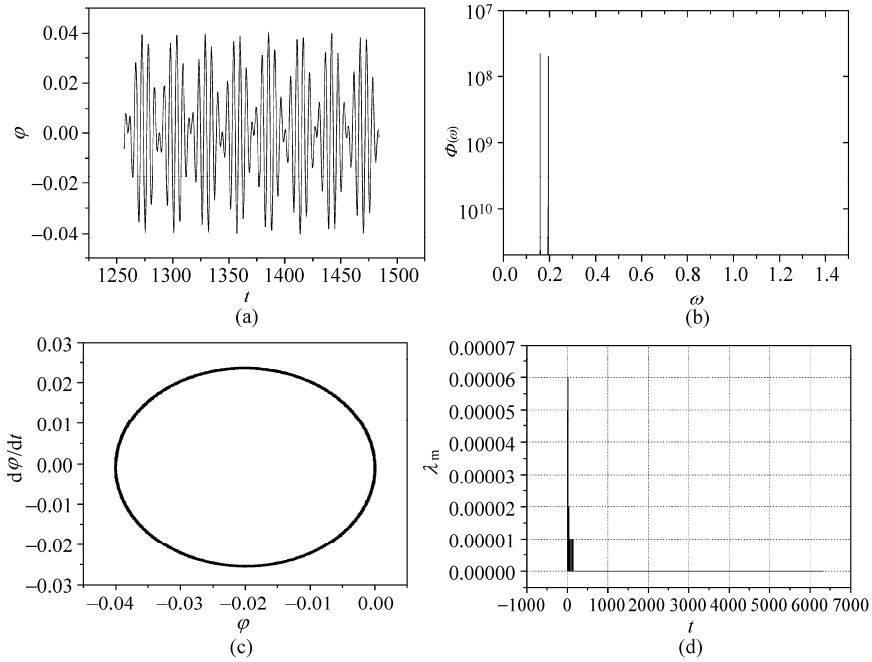

Figure 3.9 Quasi-periodic motion ($\alpha = 0.01$): (a) the time history; (b) power spectrum; (c) the Poincaré map; and (d) the largest Lyapunov exponent

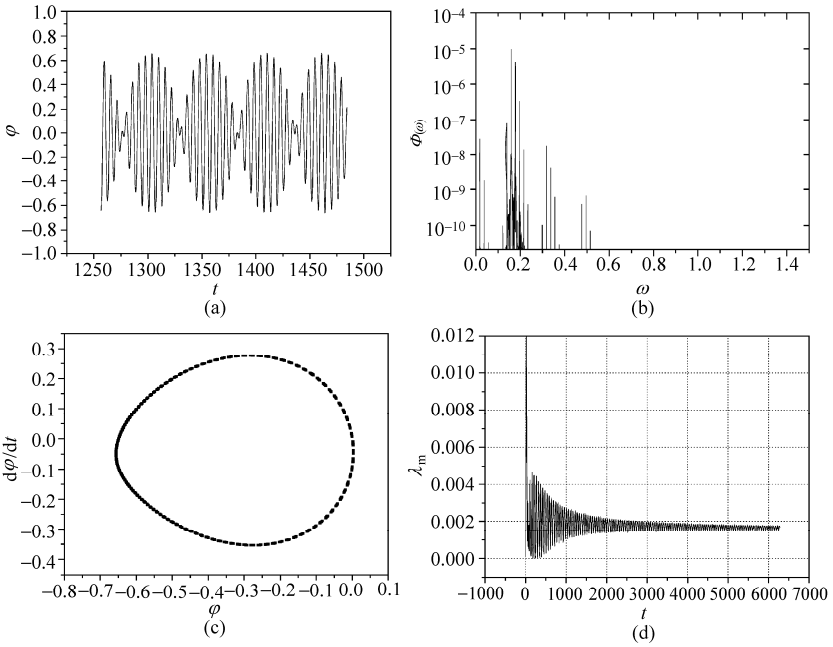

Figire 3.10 Breakup of the torus ($\alpha = 0.12$): (a) the time history; (b) power spectrum; (c) the Poincaré map; and (d) the largest Lyapunov exponent

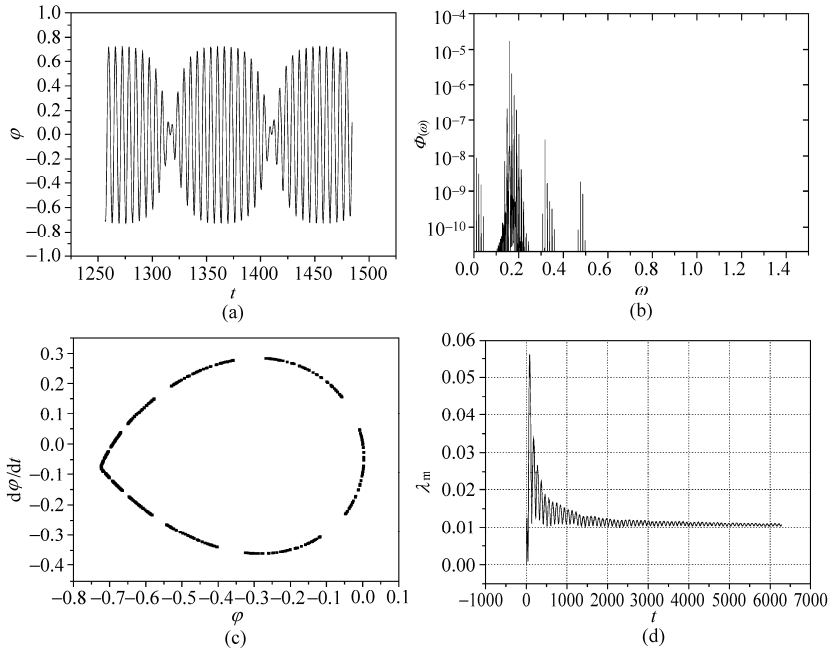

Figure 3.11 Breakup of the torus ($\alpha = 0.12175$): (a) the time history; (b) power spectrum; (c) the Poincaré map; and (d) the largest Lyapunov exponent

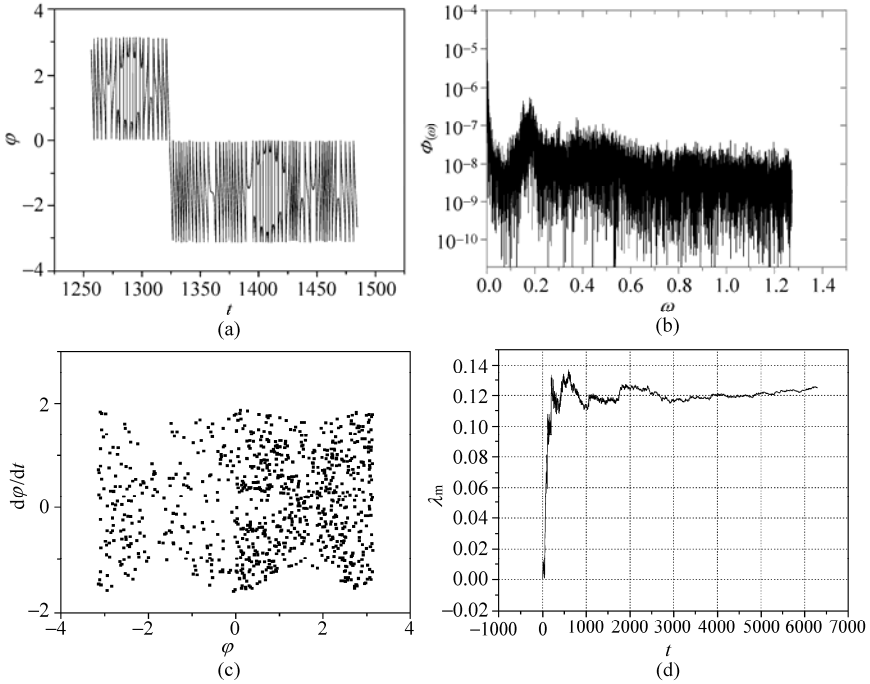

Figure 3.12 Chaotic motion ($\alpha = 0.12176$): (a) the time history; (b) power spectrum; (c) the Poincaré map; and (d) the largest Lyapunov exponent

3.3.5 Numerical Investigations: Damped Case

The effects of the magnetic parameter α and the damping coefficient γ upon the uncontrolled spacecraft attitude motion are respectively investigated numerically by integrating Eq. (3.3.6). Equation (3.3.6) can be cast into the following form

$$\begin{aligned} \dot{x}_1 &= x_2 \\ \dot{x}_2 &= -\kappa \sin 2x_1 - \gamma x_2 + \alpha(2\sin x_1 \sin x_3 + \cos x_1 \cos x_3) \\ \dot{x}_3 &= 1 \end{aligned} \tag{3.3.13}$$

The linearized system of Eqs. (3.3.13) is characterized by the Jacobian matrix

$$\begin{pmatrix} 0 & 1 & 0 \\ -2K\cos 2x_1 + \alpha(2\cos x_1 \sin x_3 - \sin x_1 \cos x_3) & \gamma & \alpha(2\sin x_1 \cos x_3 - \cos x_1 \sin x_3) \\ 0 & 0 & 0 \end{pmatrix} \tag{3.3.14}$$

which is needed in order to calculate the Lyapunov exponents. The characteristic dynamical behavior is investigated by varying the magnetic parameter α and the

damping coefficient γ, respectively, while the gravitational parameter κ is kept constant at $\kappa = 1.1$. In this case, the condition of the Melnikov theory given by Eq. (3.3.12) is $\alpha/\gamma > 1.5738$. The numerical integration begins from the initial conditions described by $(x_1, x_2, x_3)^{\mathrm{T}} = (0,0,0)$.

For a given γ, the intermittency transition accrues as the magnetic parameter α is increased. Let $\gamma = 0.2$, then the Melnikov theory requires $\alpha > 0.4452$. The dynamical behaviors of the system at $\alpha = 0.6984$, 0.6985, 0.69855,0.6986 are shown in Figs. 3.13, 3.14, 3.15, and 3.16. The corresponding Lyapunov exponents are shown in Table 3.1. As α is increased, the periodic behavior becomes the regular motion intermittently interrupted by a finite duration burst of irregular motion. For the further increase of α, the bursts become so frequent that the regular behavior can no longer be distinguished, and the chaotic motion is developed. Due to the transient behavior, the largest Lyapunov exponent is positive at the beginning of the periodic motion in Fig. 3.13. During the intermittency transition shown in Figs. 3.14 and 3.15, the motions depend sensitively on initial conditions so that the largest Lyapunov exponents are still positive in durations of the periodic motions between irregular bursts.

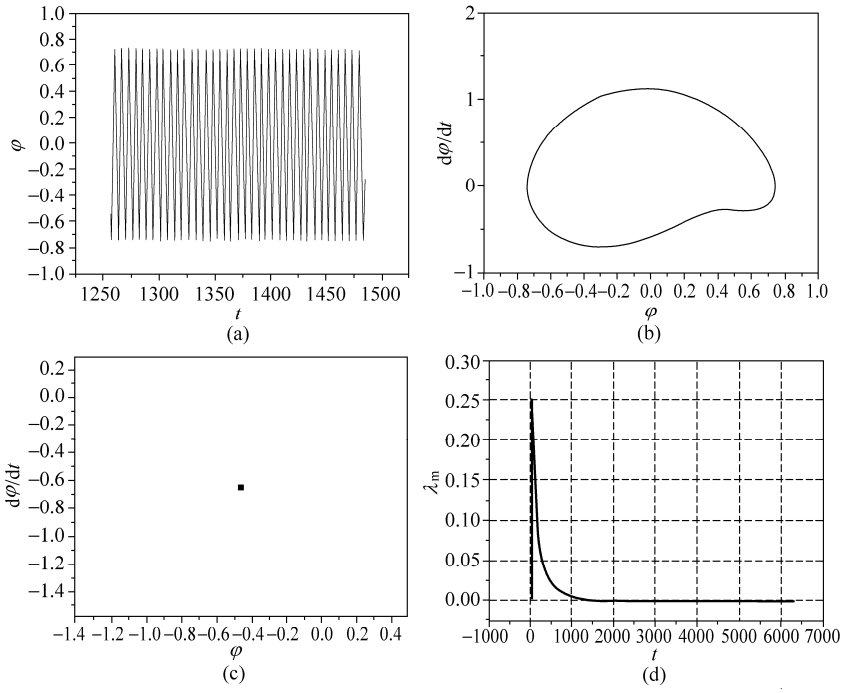

Figire 3.13 Periodic motion ($\alpha = 0.6984$, $\gamma = 0.2$): (a) the time history; (b) phase trajectory; (c) the Poincaré map; and (d) the largest Lyapunov exponent

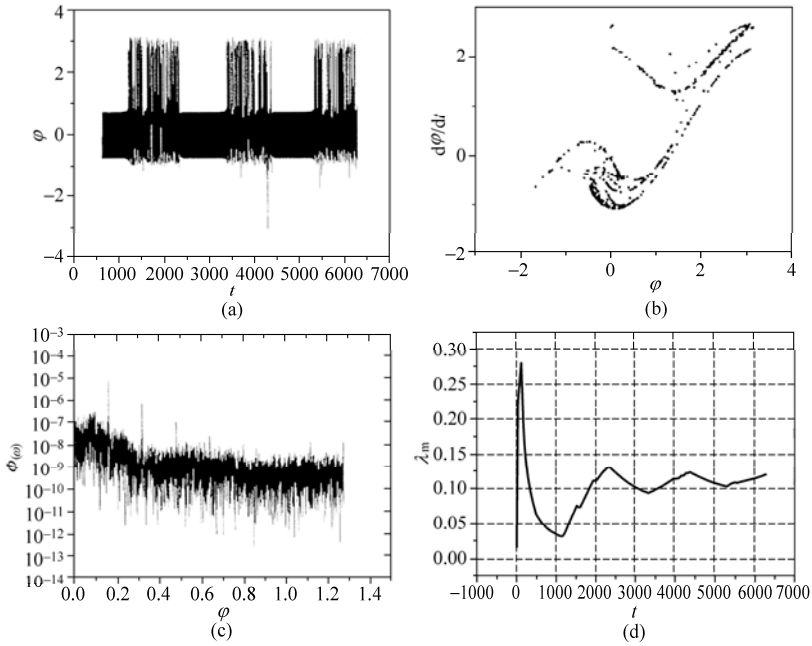

Figure 3.14 Intermittency ($\alpha = 0.6985$, $\gamma = 0.2$): (a) the time history; (b) the Poincaré map; (c) power spectrum; and (d) the largest Lyapunov exponent

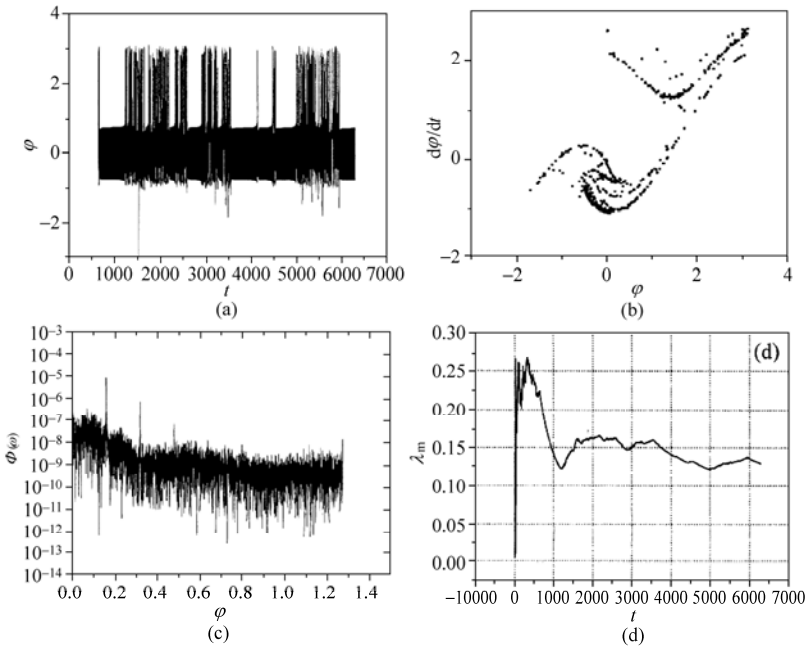

Figure 3.15 Intermittency ($\alpha = 0.69855$ $\gamma = 0.2$): (a) the time history; (b) the Poincaré map; (c) power spectrum; and (d) the largest Lyapunov exponent

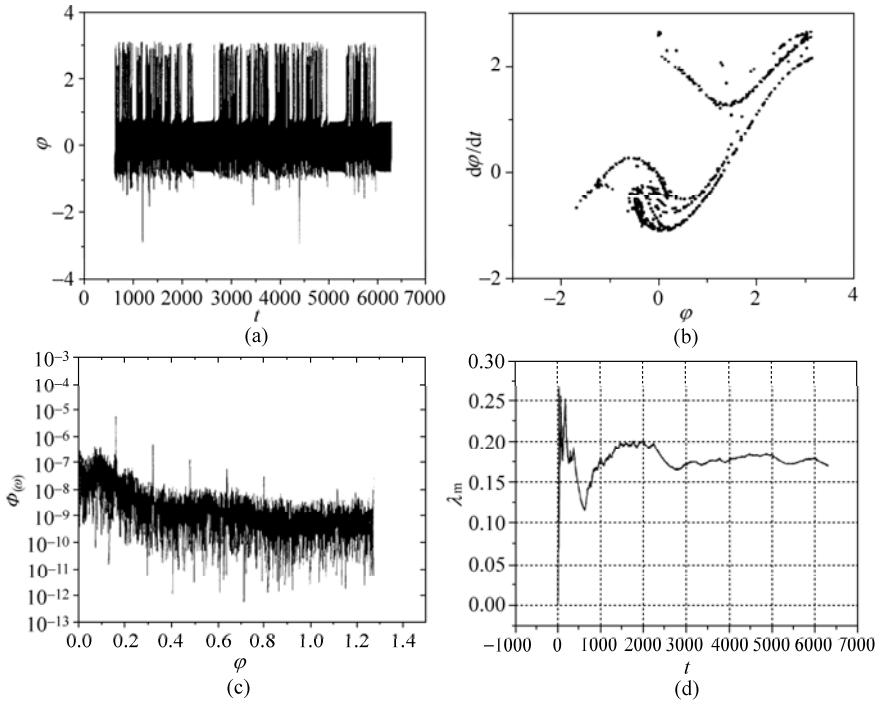

Figure 3.16 Chaotic motion ($\alpha = 0.6986$, $\gamma = 0.2$): (a) the time history; (b) the Poincaré map; (c) power spectrum; and (d) the largest Lyapunov exponent

Table 3.1 Lyapunov exponents ($\gamma = 0.2$)

α	λ_1	λ_2	λ_3
0.6984	0.00	−0.01	−0.19
0.6985	0.12	0.00	−0.32
0.69855	0.13	0.00	−0.33
0.6986	0.17	0.00	−0.37

For a given α, the intermittency transition accrues as the damping coefficient α is decreased. Let α be fixed as $\alpha = 0.7$, then the Melnikov theory requires $\gamma < 0.317$. The case that $\gamma = 0.295$, 0.290, 0.285,0.280 are shown in Figs. 3.17, 3.18, 3.19, and 3.20. The corresponding Lyapunov exponents are listed in Table 3.2.

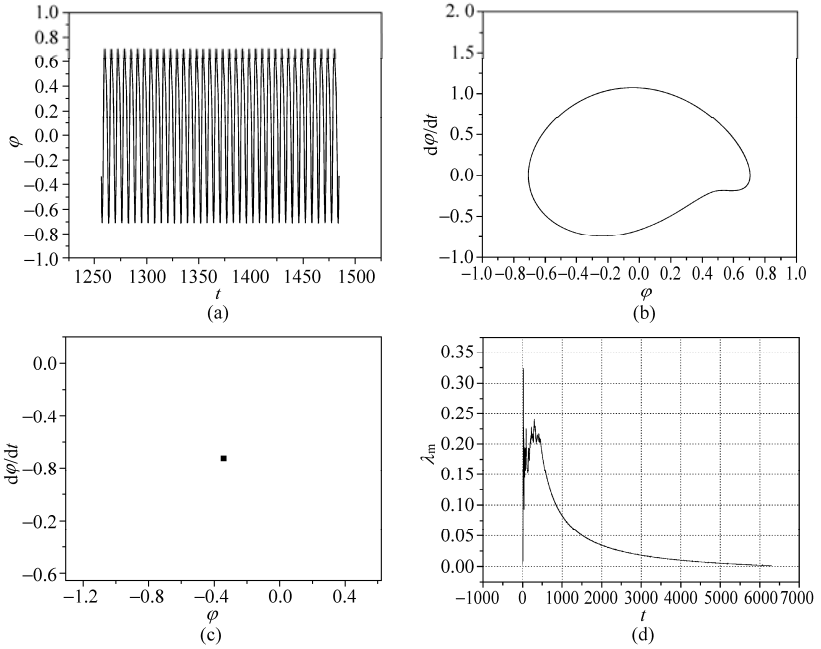

Figure 3.17 Periodic motion ($\alpha = 0.7$, $\gamma = 0.295$): (a) the time history; (b) phase trajectory; (c) the Poincaré map; and (d) the largest Lyapunov exponent

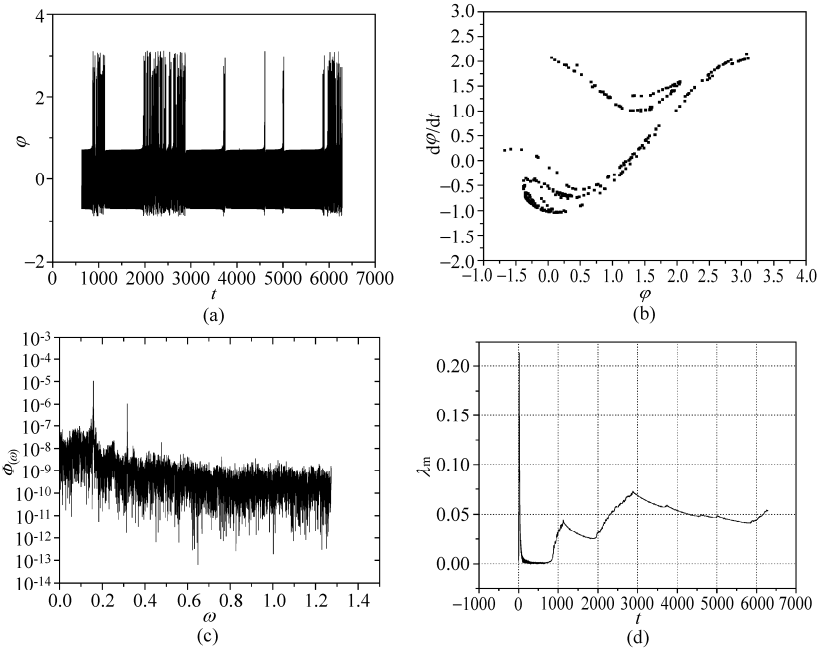

Figure 3.18 Intermittency ($\alpha = 0.7$, $\gamma = 0.290$): (a) the time history; (b) the Poincaré map; (c) power spectrum; and (d) the largest Lyapunov exponent

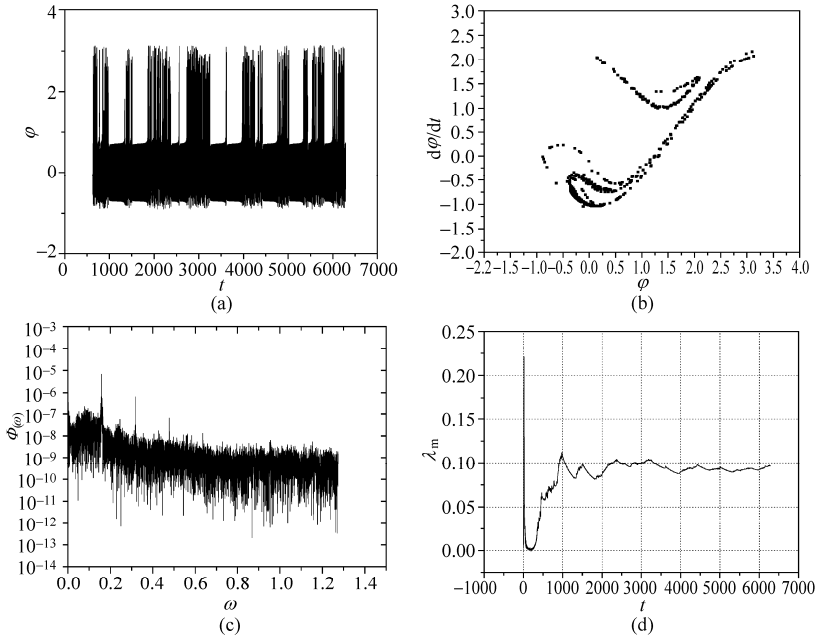

Figure 3.19 Intermittency ($\alpha = 0.7,\ \gamma = 0.285$): (a) the time history; (b) the Poincaré map; (c) power spectrum; and (d) the largest Lyapunov exponent

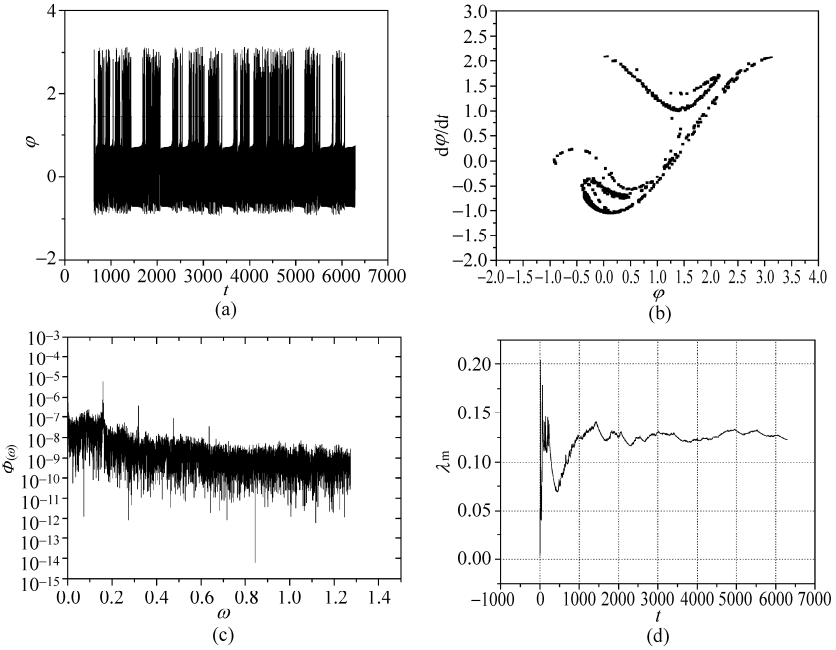

Figure 3.20 Chaotic motion ($\alpha = 0.7,\ \gamma = 0.280$): (a) the time history; (b) the Poincaré map; (c) power spectrum; and (d) the largest Lyapunov exponent

Table 3.2 Lyapunov exponents (α=0.7)

γ	λ_1	λ_2	λ_3
0.295	0.00	0.00	−0.30
0.290	0.05	0.00	−0.34
0.285	0.10	0.00	−0.38
0.280	0.12	0.00	−0.40

3.4 Magnetic Rigid Spacecraft in an Elliptic Orbit

3.4.1 Introduction

This section continues to discuss chaotic attitude motion in the gravitational and magnetic fields. The spacecraft considered here moves in an elliptic orbit instead of a circular orbit.

Although the dynamical equation for a magnetic rigid spacecraft in an elliptic orbit was established by 1985 [33], investigations of chaotic attitude motion were rather limited. Koch and Bruhn applied the Melnikov method to a polar satellite, a satellite whose orbital plane contains the symmetry axis of the central body, in an elliptic orbit under the action of the gravitational torque and the magnetic torque [3]. Liu and Chen investigated chaotic attitude motion of a magnetic rigid spacecraft with internal damping in an elliptic orbit. They used the Melnikov method to predict transverse heteroclinic cycles in the Poincaré map of the system, and employed the time history, the Poincaré map, the Lyapunov exponents and the power spectrum to identify chaos [42]. Bhardwaj and Kaur developed the Melnikov function for magnetic rigid spacecraft in an elliptic orbit and numerically showed the simple zeros of the function [43]. They also applied Chrikov's criterion [22] to estimate the half width of the chaotic separatrix and highlighted numerically the effects of the magnetic torque parameter, the orbital eccentricity, and the mass distribution parameter [44].

This section begins with modeling a magnetic rigid body spacecraft in an elliptic orbit. The Melnikov theory is applied to predict the appearance of transverse heteroclinic points. Chaotic attitude motion is numerically demonstrated via the Poincaré map, the power spectrum and the Lyapunov exponents.

3.4.2 Dynamical Model

Consider a magnetic rigid spacecraft moving in an elliptic orbit in the gravitational and magnetic field of the Earth. Assume that the inertial reference frame

(O_e-$X_0Y_0Z_0$) has the origin O_e at the mass center of the Earth, with the polar axis of the Earth as Z_0-axis and the line from O_e to the ascending node as X_0-axis. The principal coordinate frame (*O-xyz*) has the mass center *O* as the origin. Principal moments of inertia of the arbitrarily shaped spacecraft are *A*, *B* and *C*. Suppose that *B*>*A*. The orbital coordinate frame (*O-XYZ*) is established with the radial vector from O_e to *O* as *X*-axis, the normal vector to orbital plane *XY* as *Z*-axis. The base vectors of (*O-XYZ*) are $\boldsymbol{i}$, $\boldsymbol{j}$, $\boldsymbol{k}$. Denote φ as the libration angle in the orbital plane with respect to *X*- or *Y*-axes, ν as the true anomaly of the spacecraft as the position angle measured from perigee, and *i* as the angle of inclination of the orbital plane, and ω is the argument of perigee, all shown in Fig. 3.7.

The theorem of angular momentum about the center of mass is still expressed by Eq. (3.3.2), in which $\boldsymbol{G}$ is the angular momentum, $\boldsymbol{M}_g$ and $\boldsymbol{M}_m$ are the gravitational and magnetic torques, respectively, and $\boldsymbol{M}_d$ is the internal damping torque proportional to the angular velocity with coefficient *c*.

For planar libration, all vectors in Eq. (3.3.2) are along the normal axis of the orbital plane. The magnitudes of torques $\boldsymbol{M}_g$ and $\boldsymbol{M}_d$ are given by Eqs. (1.3.12) and (3.3.1), respectively. The components of the magnetic flux density $\boldsymbol{H}_m$ of the Earth in (*O-XYZ*) are given by Eq. (1.2.11). For the elliptic orbit, the orbital angle *u* in Eq. (1.2.11) can be expressed by Eq. (1.1.29). Assume that the magnetic moment $\boldsymbol{I}_m$ of the spacecraft is along *Ox*-axis and the direction of the vector $\boldsymbol{I}_m$ in the orbital plane is specified by the angle φ as shown in Fig. 1.11. Thus the direct cosines of $\boldsymbol{I}_m$ with respect to (*O-XYZ*) are ($\cos\varphi$, $\sin\varphi$, 0). Substitution of Eqs. (1.2.9) and (1.2.11) with $H_{m0} = \mu_m / r^3$ and the direct cosines into Eq. (1.2.14) yields the projection of the magnetic torque $\boldsymbol{H}_m$ on *Oz*-axis as

$$M_{mZ} = \frac{I_m \mu_m}{2r^3} \sin i (3\cos(\varphi - \nu - \omega) - \cos(\varphi + \nu + \omega)) \tag{3.4.1}$$

where *r* is distance between *O* and O_e, and μ_m is the Earth magnetic dipole strength. Projection of Eq. (3.3.2) on the *Oz*-axis and substitution of Eqs. (3.3.1), (1.3.12) and (3.4.1) into the resulting equation leads to

$$\begin{aligned} C\left(\frac{\mathrm{d}^2\varphi}{\mathrm{d}t^2} + \frac{\mathrm{d}^2\nu}{\mathrm{d}t^2}\right) = &-\frac{3\mu}{2r^3}(B - A)\sin 2\varphi \\ &+ \frac{I_m \mu_m}{2r^3} \sin i (3\cos(\varphi - \nu - \omega) - \cos(\varphi + \nu + \omega)) - c\frac{\mathrm{d}\varphi}{\mathrm{d}t} \end{aligned} \tag{3.4.2}$$

where μ is the gravitational attraction constant of the Earth.

The orbital motion and the attitude motion are assumed to be decoupled. The effect of the magnetic field on the orbital motion is neglected. The spacecraft undergoes the Kepler motion expressed by Eqs. (1.3.24). Substitution of Eqs. (1.3.24) and (1.3.25) into Eq. (3.1.1) yields dynamical model of a magnetic rigid

spacecraft in an elliptic orbit

$$\ddot{\varphi}-\frac{2e\sin\nu}{1+e\cos\nu}(1+\dot{\varphi})+\frac{\kappa\sin 2\varphi}{1+e\cos\nu}+\frac{\gamma}{(1+e\cos\nu)^2}\dot{\varphi}-\alpha\frac{\cos(\varphi+\nu+\omega)-3\cos(\varphi-\nu-\omega)}{1+e\cos\nu}=0 \tag{3.4.3}$$

where

$$\kappa=\frac{3(B-A)}{2C},\quad \alpha=\frac{I_{\mathrm{m}}\mu_{\mathrm{m}}}{2C\mu}\sin i,\quad \gamma=\frac{cp\sqrt{p}}{C\sqrt{\mu}} \tag{3.4.4}$$

p is the semi-parameter of the orbit, e is the orbit eccentricity, and the over dot denotes the derivative with respect to the position angle ν.

3.4.3 Melnikov Analysis

Since e, α, and γ are all small, introduce a small dimensionless parameter $\varepsilon\,(0<\varepsilon\ll 1)$ such that $e=\varepsilon e_1$, $\alpha=\varepsilon\alpha_1$, $\gamma=\varepsilon\gamma_1$. Retaining the first order terms of ε and omitting the higher order terms in Eq. (3.4.3) lead to an integrable Hamiltonian system under small perturbations

$$\begin{aligned}\ddot{\varphi}+\kappa\sin 2\varphi=\varepsilon[&2e_1\sin\nu(1+\dot{\varphi})+e_1\kappa\cos\nu\sin 2\varphi\\&+\alpha_1(\cos(\varphi+\nu+\omega)-3\cos(\varphi-\nu-\omega))-\gamma_1\dot{\varphi}]\end{aligned} \tag{3.4.5}$$

If $\varepsilon=0$, Eq. (3.4.5) becomes Eq. (3.1.4) with two hyperbolic saddle points $(\pm\pi/2,\,0)$ connected by the heteroclinic orbits $\Gamma^{\pm}$ defined by Eq. (3.1.9). For $\varepsilon\neq 0$, Eq. (3.4.5) can be cast into the form of Eq. (2.3.4) with

$$\boldsymbol{x}=\begin{pmatrix}\varphi\\ \dot{\varphi}\end{pmatrix},\quad \boldsymbol{f}(\boldsymbol{x})=\begin{pmatrix}\dot{\varphi}\\ \kappa\sin 2\varphi\end{pmatrix}$$

$$\boldsymbol{g}(\boldsymbol{x},\nu)=\begin{pmatrix}0\\ 2e_1\sin\nu(1+\dot{\varphi})+e_1\kappa\cos\nu\sin 2\varphi+\alpha_1(\cos(\varphi+\nu+\omega)-3\cos(\varphi-\nu-\omega))-\gamma_1\dot{\varphi}\end{pmatrix} \tag{3.4.6}$$

Equation (2.3.26) yields

$$\begin{aligned}\mathcal{M}_{\pm}(\nu_0)=\int_{-\infty}^{+\infty}\big[&2e_1\sin(\nu+\nu_0)(1+\dot{\varphi}_{\pm}(\nu))+e_1\kappa\cos(\nu+\nu_0)\sin 2\varphi_{\pm}(\nu)-\gamma_1\dot{\varphi}_{\pm}(\nu)\\&+\alpha_1(\cos(\varphi_{\pm}(\nu)+\nu+\nu_0+\omega)-3\cos(\varphi_{\pm}(\nu)-\nu-\nu_0-\omega))\big]\dot{\varphi}_{\pm}(\nu)\,\mathrm{d}\nu\end{aligned} \tag{3.4.7}$$

Substitution of Eq. (3.1.9) into Eq. (3.4.7) and calculation of the resulting integrals

yield the Melnikov function

$$\begin{aligned}\mathcal{M}_{\pm}(\tau_0) = \frac{\pi}{2} e_1 \left(\mp 4 \operatorname{sech} \frac{\pi}{2\sqrt{2\kappa}} + 3 \operatorname{csch} \frac{\pi}{2\sqrt{2\kappa}} \right) \sin \nu_0 \\ + \alpha_1 \pi \left(\frac{1+\sqrt{2\kappa}}{2\kappa} \right) \operatorname{csch} \left(\frac{\pi}{2\sqrt{2\kappa}} \right) \sin(\nu_0 + \omega) - 2\sqrt{2}\gamma_1 \kappa\end{aligned} \tag{3.4.8}$$

Hence $\mathcal{M}_{\pm}(\nu_0)$ has simple zeros on the condition that

$$\gamma < \frac{\sqrt{2}\,\pi}{8\kappa} \sqrt{A^2 + B^2} \tag{3.4.9}$$

where

$$\begin{aligned}A &= e\left(-4 \operatorname{sech} \frac{\pi}{2\sqrt{2\kappa}} + 3 \operatorname{csch} \frac{\pi}{2\sqrt{2\kappa}} \right) + \alpha \left(\frac{1+\sqrt{2\kappa}}{\kappa} \right) \operatorname{csch} \left(\frac{\pi}{2\sqrt{2\kappa}} \right) \cos \omega \\ B &= \alpha \left(\frac{1+\sqrt{2\kappa}}{\kappa} \right) \operatorname{csch} \left(\frac{\pi}{2\sqrt{2\kappa}} \right) \sin \omega\end{aligned} \tag{3.4.10}$$

3.4.4 Numerical Simulations

Chaotic attitude motion of the spacecraft can be numerically demonstrated by integrating Eq. (3.4.3) which is rewritten as

$$\begin{aligned}\frac{\mathrm{d}x_1}{\mathrm{d}\nu} &= x_2 \\ \frac{\mathrm{d}x_2}{\mathrm{d}\nu} &= \frac{2e \sin x_3}{1 + e\cos x_3}(1 + x_2) - \frac{\kappa \sin 2x_1}{1 + e\cos x_3} - \frac{\gamma}{(1 + e\cos x_3)^2} x_2 \\ &\quad - \alpha \frac{3\cos(x_1 - x_3 - \omega) - \cos(x_1 + x_3 + \omega)}{1 + e\cos x_3} \\ \frac{\mathrm{d}x_3}{\mathrm{d}\nu} &= 1\end{aligned} \tag{3.4.11}$$

where

$$x_1 = \varphi, \quad x_2 = \frac{\mathrm{d}\varphi}{\mathrm{d}\nu}, \quad x_3 = \nu \tag{3.4.12}$$

Various tools including the time history, Poincaré map, Lyapunov exponents and power spectrum are used to identify the dynamical behavior. The linearized system of Eq. (3.4.11) is characterized by the Jacobian matrix

$$\boldsymbol{A}=\begin{pmatrix} 0 & 1 & 0 \\ a_{21} & a_{22} & a_{23} \\ 0 & 0 & 0 \end{pmatrix} \tag{3.4.13}$$

where

$$\begin{aligned} a_{21} &= -\frac{2\kappa\cos 2x_1}{1+e\cos x_3}+\alpha\frac{3\sin(x_1-x_3-\omega)-\sin(x_1+x_3+\omega)}{1+e\cos x_3} \\ a_{22} &= \frac{2e\sin x_3}{1+e\cos x_3}-\frac{\gamma}{(1+e\cos x_3)^2} \\ a_{23} &= \frac{2e(e+\cos x_3)}{(1+e\cos x_3)^2}(1+x_2)-\frac{e\kappa\sin 2x_1\sin x_3}{(1+e\cos x_3)^2}-\frac{2e\gamma\sin x_3}{(1+e\cos x_3)^3}x_2 \\ &\quad -\alpha\frac{3\sin(x_1-x_3-\omega)+\sin(x_1+x_3+\omega)}{1+e\cos x_3} \\ &\quad -\alpha\frac{e\sin x_3\left[3\cos(x_1-x_3-\omega)-\cos(x_1+x_3+\omega)\right]}{(1+e\cos x_3)^2} \end{aligned} \tag{3.4.14}$$

The numerical integration begins from the initial conditions $(x_1, x_2, x_3)^{\mathrm{T}} = (0, 0, 0)^{\mathrm{T}}$ at $\nu = 0$.

Let successively

$$e=0.8,\ K=1.1,\ \gamma=0.1,\ \alpha=0.9,\ \omega=1.2 \tag{3.4.15}$$

$$e=0.4,\ K=1.0,\ \gamma=0.2,\ \alpha=0.7,\ \omega=0.1 \tag{3.4.16}$$

Chaos occurs in both cases. Their time histories, Poincaré maps, the largest Lyapunov exponents and power spectrums are shown in Figs. 3.21 and 3.22. Lyapunov exponents of chaos (3.4.15) are 0.55, 0.00 and −1.01. Lyapunov exponents of chaos (3.4.16) are 0.39, 0.00 and −0.65.

If e is small, chaos still appears due to the magnetic torque. For example, let

$$e=0.04,\ K=1.0,\ \gamma=0.2,\ \alpha=0.7,\ \omega=0.1 \tag{3.4.17}$$

The time histories, Poincaré map, the largest Lyapunov exponent and power spectrums are shown in Fig. 3.23. Lyapunov exponents in this case are 0.33, 0.00 and −0.52.

However, if both e and α are small, periodic motion appears. For example, let

$$e=0.08,\ K=1.1,\ \gamma=0.1,\ \alpha=0.09,\ \omega=1.2 \tag{3.4.18}$$

The phase trajectory and the largest Lyapunov exponent are shown in Fig. 3.24. The Lyapunov exponents in this case are 0.00, −0.05 and −0.05.

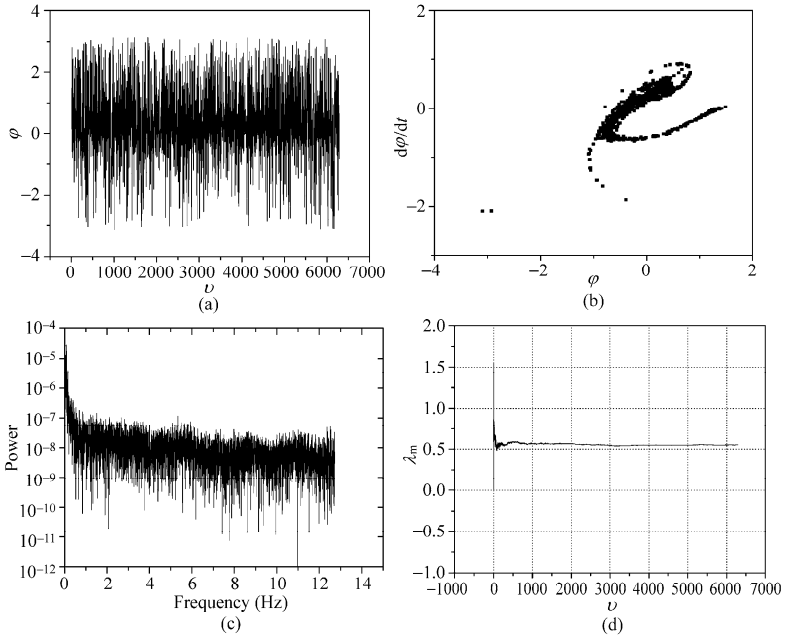

Figire 3.21 Chaos (3.4.16): (a) the time history; (b) the Poincaré map; (c) power spectrum; and (d) the largest Lyapunov exponent

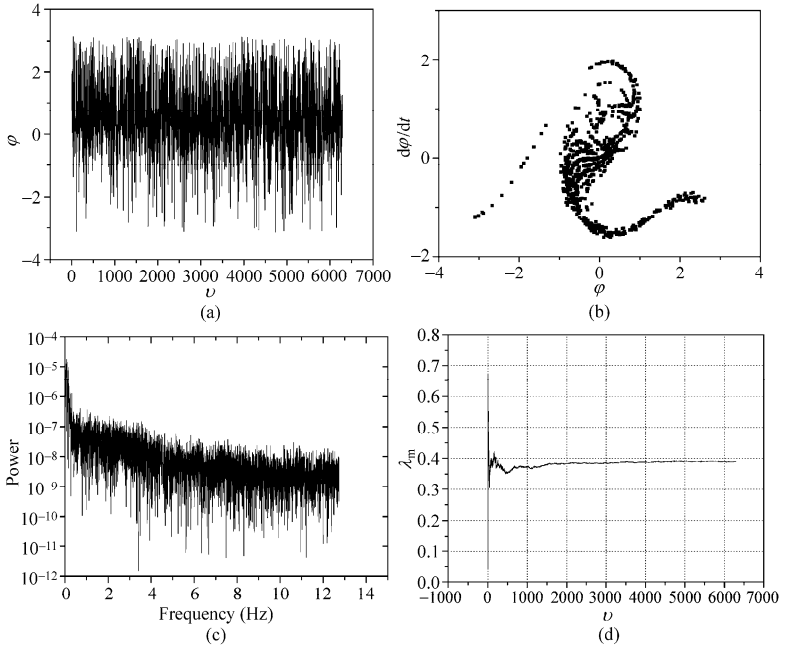

Figure 3.22 Chaos (3.4.17): (a) the time history; (b) the Poincaré map; (c) power spectrum; and (d) the largest Lyapunov exponent

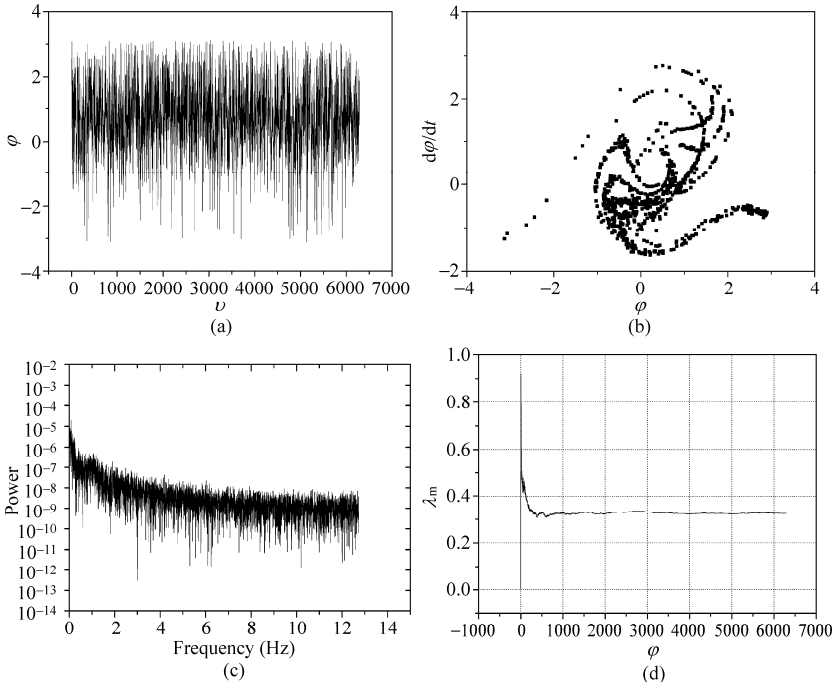

Figure 3.23 Chaos (3.4.17): (a) the time history; (b) the Poincaré map; (c) power spectrum; and (d) the largest Lyapunov exponent

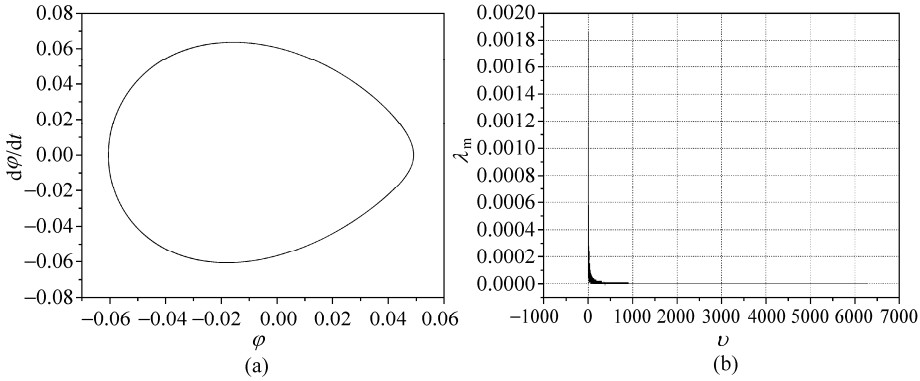

Figure 3.24 Periodic motion: (a) the time history; and (b) the largest Lyapunov exponent

References

[1] Gouliaev VI, Zubritska AL, Koshkin VL. Universal sequence of period-doubling bifurcation of satellite vibrations in an elliptical orbit. *Mechanics of Solids*, 1989, 24(3), 5-10

[2] Seisl M, Steindl AL. Chaoticsche schwingungen von satelliten. *Zeitschrift für Angewandte Mathematik und Mechanik*, 1989, 69, 352-354

[3] Koch BP, Bruhn B. Chaotic and periodic motions of satellites in elliptic orbits. *Zeitschrift für Naturforschung. Teil A*, 1989, 44, 1155-1162

[4] Chen LQ, Liu YZ. Chaotic attitude motion of a class of spacecrafts on an ellipic orbit. *Technische Mechanik*, 1998, 18, 41-44

[5] Beletsky VV. *Regular und Chaotisch Bewegung Sturrer Korper*. Berlin: Teubner-Verlag, 1995

[6] Beletsky VV, Pivovarov ML, Starostin EL. Regular and chaotic motions in applied dynamics of a rigid body, *Chaos*, 1996, 6(2), 155-166

[7] Khan A, Sharma R, Saha L M. Chaotic motion of an ellipsoidal satellite. *The Astronomical Journal*, 1998, 116, 2058-2066

[8] Richardson DL, Bartler T. Chaos in artificial satellite motion due to third-body effects. *Advances in the Astronautical Sciences,* 1995, 90(3), 1685-1700

[9] Ashenberg J(1996), Satellite pitch dynamics in the elliptic problem of three bodies, *Journal of Guidance, Control, and Dynamics*, 19(1), 68-74

[10] Bhardwaj R, Bhatnagar KB. Chaos in nonlinear planar oscillation of a satellite in an elliptical orbit under the influence of third body torque. *Indian Journal of Pure & Applied Mathematics*, 1997, 28 (3), 391-422

[11] Bhardwaj R, Tuli R. Chaos in attitude motion of a satellite under a third body torque in an elliptic orbit. *Indian Journal of Pure and Applied Mathematics*, 2003, 34 (2), 277-289

[12] Mehra VI, Bhatnagar KB. Planar oscillation of a satellite in an elliptic orbit under the influence of solar-radiation pressure and 3rd body torque. *Indian Journal of Pure and Applied Mathematics*, 1995, 26 (7), 725-742

[13] Stabb MC, Gray GL. Chaos in controlled, gravity gradient satellite pitch dynamics via the method of Melnikov-center stabilization, *Advances in the Astronautical Sciences,* 1993, 82(1), 147-166

[14] Gray GL, Stabb MC. Chaos in controlled, gravity gradient satellite pitch dynamics via the method of Melnikov-saddle stabilization. *Advances in the Astronautical Sciences*, 1993, 84(1), 441-449

[15] Toniolo MD, Lee M, Gray GL. Comparison of Melnikov's method and numerical simulation for predicting nonlinear dynamics in the pitch motion of actively controlled satellites in a gravity gradient field. *Advances in the Astronautical Sciences, Astrodynamics*, 1999, 103(2), 1159-1178

[16] Gouliaev VI, Zubritska AL and Koshkin VL. Universal sequence of period-doubling bifurcations for a satellite generated from the unstable steady state. *Mechanics of Solids*, 1991, 26(1), 8-12

[17] Gouliaev VI, Zavrazhina TV. Universal similarities of transition to chaos of satellite oscillation in elliptic orbit. *International Journal of Non-Linear Mechanics*, 1998, 33(2), 215-226

[18] Tong X, Rimrott FPJ. Numerical studies on chaotic planar motion of satellites in an elliptic orbit, *Chaos Solitons Fractals*, 1991, 1(2), 179-186

[19] Karasopoulos HA, Richardson DL. Numerical investigation of chaos in the attitude motion of a gravity-gradient satellite, *Advances in the Astronautical Sciences,* 1993, 85(3), 1851-1870

[20] Teofilatto P, Graziani F. On librational motion of spacecraft, *Chaos, Solitons and Fractals*, 1996, 7(10), 1721-1744

[21] Kirchgraber U, Manz U, Stoffer D. Rigorous proof of chaotic behaviour in a dumbbell satellite model. *Journal of Mathematical Analysis and Applications*, 2000, 251, 897-911

[22] Chirikov BV. A universal instability of many-dimensional oscillator systems. *Physics Reports*, 52,5(1979): 263-379

[23] Beletsky VV, Levin EM. *Dynamics of Space Tether Systems*, American Astronautical Society, San Diego, 1993

[24] Nixon MS, Misra AK. Nonlinear dynamics and chaos of two-body tethered satellite systems, *Advances in the Astronautical Sciences,* 1993, 85(1), 775-794

[25] Peng JH, Liu YZ. Chaotic motion of the tethered satellite system. *Technische Mechanik*, 1996, 16(4), 327-331

[26] Béda PB. On saddle-node bifurcation and chaos of satellites, *Nonlinear Analysis, Theory, Methods, & Applications*, 1997, 30(8), 4881-4886

[27] Fujii HA, Ichiki W. Nonlinear dynamics of the tethered subsatellite system in the station keeping phase, *Journal of Guidance, Control, and Dynamic*, 1997, 20(2), 403-406

[28] Steiner W. Transiently chaotic movements of tethered satellite systems, *Zeitschrift fuer Angewandte Mathematik und Mechanik*, 1997, 77(S1), 323-324

[29] Steiner W. Transient chaotic oscillations of a tethered satellite system. *Acta Mech.*, 1998, 127, 155-163

[30] Beletsky VV, Pivovarov ML. The effect of the atmosphere on the attitude motion of a dumb-bell-shaped artificial satellite, *Journal of Applied Mathematics and Mechanics*, 2000, 64(5), 691-670

[31] Misra AK, Nixon MS, Modi VJ. Nonlinear dynamics of two-body tethered satellite systems: Constant length case. *Journal of the Astronautical Sciences*, 2001, 49 (2), 219-236

[32] Takeichi N, Natori MC, Okuizumi N. Dynamics behavior of a tethered system with multiple subsatellites in elliptic orbits. *Journal of Spacecraft and Rockets*, 2001, 38, 914-921

[33] Beletsky VV, Hentov AA. *Rotational Motion of a Magnetized Satellite*. Moscow: Moscow University Press, 1985 (in Russian)

[34] Bhardwaj R, Bhatnagar KB, Nonlinear planar oscillation of a satellite in circular orbit under the influence of magnetic torque 1. *Indian Journal of Pure & Applied Mathematics*, 1995, 26(12), 1225-1240

[35] Bhardwaj R, Bhatnagar KB. Nonlinear planar oscillation of a satellite in circular orbit under the influence of magnetic torque 2. *Indian Journal of Pure & Applied Mathematics*, 1998, 29(2), 139-150

[36] Beletsky VV, Lopes RVF, Pivovarov M. Chaos in spacecraft attitude motion in Earth's magnetic field, *Chaos*, 1999, 9(2), 493-498

[37] Cheng G, Liu YZ. Chaotic motion of a magnetic rigid satellite in an orbit near the equatorial plane of the earth. *Technische Mechanik*, 1999, 19(3) , 199-201

[38] Chen LQ, Liu YZ, Cheng G. Chaotic attitude motion of a magnetic rigid spacecraft in a circular orbit near the equatorial plane, *Journal of The Franklin Institute*, 2002, 339(1) , 121-128

[39] Chen LQ, Liu YZ. Chaotic attitude motion of a magnetic rigid spacecraft and its control. *International Journal of Non-Linear Mechanics*, 2002, 37(3) , 493-504

[40] Morales-Ruiz JJ. *Differential Galois Theory and Non-integrability of Hamiltonian Systems*. Basel: Birkhäuser, 1999

[41] Maciejewski AJ, Przybylska M. Non-integrability of the problem of a rigid satellite in gravitational and magnetic fields. *Celestial Mechanics and Dynamical Astronomy*, 2003, 87, 317-351

[42] Liu YZ, Chen LQ. Chaotic attitude motion of a magnetic rigid spacecraft in an elliptic orbit and its control, *Acta Mechanica Sinica*, 2003, 19(1), 71-78

[43] Bhardwaj R, Kaur P. Satellite's motion under the effect of magnetic torque. *American Journal of Applied Sciences*, 2006, 3, 1899-1902

[44] Bhardwaj R, Kaur P. Chaotic attitude tumbling of satellite in magnetic field. *American Journal of Applied Sciences*, 2006, 3, 2037-2041

[45] Wiggins S. *Global Bifurcations and Chaos: Analytical Methods*. Berlin: Springer-Verlag, 1988